Fluctuation of radiation emission near a parametric instability

Bachelor's Thesis

Submitted to the Faculty of Mathematics, Computer Science and Natural Sciences at RWTH Aachen University

presented by

Apostolos Siskou

under the supervision of

Prof. Dr. Fabian Hassler
and
Prof. Dr. Markus Müller
JARA-Institute for Quantum Information

07/2023

Abstract

This thesis deals with the radiation statistics of a parametrically driven harmonic oscillator interacting with a thermalized environment. The system evolves according to the Lindblad master equation. Strong driving can lead to an exponentially increasing photon current, but a nonlinear additional potential stabilizes the system above threshold. We determine how the photon current evolves during the approach of the steady state and how detuning and temperature influence its stationary value. The correlation and fluctuation of the emitted radiation is characterized through the second-order coherence function and the Fano factor. Around a critical driving strength, the radiation rapidly turns antibunched. Close to threshold, we verify that the Fano factor has a universal form. Furthermore, an approach for a more efficient simulation method based on the decay rates of the system's modes is introduced.

Contents

Chapter 1

Introduction

The oscillations of a damped harmonic oscillator can be sustained in different ways, one of which is parametric driving at twice its natural frequency. In classical terms, the difference compared to coherent driving through an externally applied force is that the parameters of the oscillator itself are varied periodically. Applications of parametric driving include low-noise parametric amplifiers. They can be used to create squeezed light and entangled photons, as shown in Ref. [1] and Ref. [2].

In this thesis, we examine a quantum mechanical parametrically driven oscillator interacting with its environment through the emission and absorption of photons. To that end, we derive its Hamiltonian with the rotating frame approximation in Ch. 2. In the same chapter, we introduce the Lindblad master equation, which describes the dynamics of open quantum systems. Ch. 3 deals with the photon current emanating from the system which can be measured by a detector. We establish the existence of a threshold above which the radiation emission increases exponentially and show that the system is stabilized by a nonlinear term. Also, the complete time evolution of the photon current is determined, which contains the characteristic time scale at which the steady state is reached. In Ch. 4, the concept of the second-order coherence is presented and used to determine how the system parameters influence the correlation of emitted photons. We find that the statistical properties of the radiation change rapidly around a critical driving strength, above which the light is antibunched. This point shifts when the temperature and detuning are altered, which we explain qualitatively. The fluctuation of total photon counts is determined in Ch. 5 through the Fano factor. We discuss its interpretation as the total number of correlated photons and verify universal scaling laws close to threshold derived in Ref. [3]. Finally, in Ch. 6, a Bogoliubov transformation is used to extract the modes of the Liouvillian. They can be utilized for a more efficient method of simulating the Lindblad equation below threshold. It consists of only considering slowly decaying modes for the description of the system dynamics. This decreases the calculation time for obtaining accurate simulation results. Approaches for how to extend the method to driving strengths above threshold are also put forward.

Different numerical methods are introduced throughout all chapters wherever necessary. Because of its conceptual importance, the vectorization of the density operator is explained in greater detail in App. A.

Chapter 2

Setup

2.1 Parametrically driven oscillator

The classical differential equation for a parametrically driven, one-dimensional harmonic oscillator is given by

$$\ddot{x}(t) + \gamma\dot{x}(t) + x(t)\left[\omega_0^2 + 2\epsilon\omega_0 \sin(2\omega_D t)\right] = 0, \tag{2.1}$$

where ω_0 is its natural frequency and γ is the damping rate. The term in brackets can be viewed as the square of a time-dependent frequency $\omega(t)$. It oscillates around ω_0^2 with a driving frequency of $\omega_D = \omega_0 + \frac{\Delta}{2}$. The parameter $\Delta \ll \omega_0$ is called detuning and is introduced to account for slight deviations of ω_D from twice the natural frequency. Without the time dependence of $\omega(t)$, the result for weak damping ($\gamma \ll \omega_0$) would be an exponentially decaying harmonic oscillation.
The common physical example of this type of driving is a pendulum which periodically shifts its center of mass away from and toward the pivot, just like a child does when switching between standing up and crouching on a swing. The ansatz to solve Eq. 2.1 is a linear combination of harmonic terms with detuned natural frequency, i.e.

$$x(t) = x_1(t)\cos(\omega_D t) + x_2(t)\sin(\omega_D t), \tag{2.2}$$

in which the amplitudes themselves are time dependent. This ansatz is inserted into the differential equation and the second derivatives of x_1 and x_2 can be ignored under the assumption that the amplitudes change over much larger time scales than ω_0^{-1}. Doing this leads to terms of the form $\cos(\omega_D t)\sin(2\omega_D t) = \frac{1}{2}[\sin(\omega_D t) + \sin(3\omega_D t)]$ and $\sin(\omega_D t)\sin(2\omega_D t) = \frac{1}{2}[\cos(\omega_D t) - \cos(3\omega_D t)]$. The rotating wave approximation (RWA) consists in omitting the terms with frequency $3\omega_D$ because they are off-resonant and average out over the the regarded time scales. Furthermore, only terms up to the first order in $\gamma\omega_0^{-1}$ and $\Delta\omega_0^{-1}$ are retained for weak damping and detuning. The resulting differential equation only has terms proportional to either $\sin(\omega_D t)$ or $\cos(\omega_D t)$. Separately setting them equal to 0 yields a system of linear ODEs for $x_1(t)$ and $x_2(t)$ given by

$$\frac{d}{dt}\begin{pmatrix} x_1(t) \\ x_2(t) \end{pmatrix} = \begin{pmatrix} -\frac{\gamma-\epsilon}{2} & -\frac{\Delta}{2} \\ \frac{\Delta}{2} & -\frac{\gamma+\epsilon}{2} \end{pmatrix}\begin{pmatrix} x_1(t) \\ x_2(t) \end{pmatrix}. \tag{2.3}$$

Interpreting x_1 and x_2 as the two degrees of freedom in the system's phase space, Eq. 2.3 can be rewritten in the form of Hamilton's equations as

$$\begin{aligned} \dot{x}_1 &= -\frac{\gamma}{2}x_1 - \frac{\partial \mathcal{H}}{\partial x_2}, \\ \dot{x}_2 &= -\frac{\gamma}{2}x_2 + \frac{\partial \mathcal{H}}{\partial x_1}, \\ H &= -\frac{\epsilon}{2}x_1 x_2 + \frac{\Delta}{4}(x_1^2 + x_2^2) \end{aligned} \tag{2.4}$$

with additional dissipative terms proportional to γ in the equations. x_1 therefore acts as the canonical momentum, and x_2 as the coordinate. As per usual for the transition to a quantum mechanical Hamiltonian, it is convenient to express its classical version as

$$H = \frac{\Delta}{2}\alpha^*\alpha + i\frac{\epsilon}{4}(\alpha^{*2} - \alpha^2) \tag{2.5}$$

after defining the complex linear combination $\alpha = \frac{1}{\sqrt{2}}(x_2 + ix_1)$. The Hamiltonian operator is then given by

$$\hat{H} = \frac{\Delta}{2}\hat{a}^\dagger\hat{a} + i\frac{\epsilon}{4}(\hat{a}^{\dagger 2} - \hat{a}^2), \tag{2.6}$$

where α^* and α have been replaced by the creation and annihilation operators $\hat{a}^\dagger$ and $\hat{a}$. Their definition is the same, except that the numbers x_1 and x_2 are replaced by operators fulfilling the canonical commutation relation $[\hat{x}_2, \hat{x}_1] = i\hat{1}$. The commutation relation of $\hat{a}$ and $\hat{a}^\dagger$ as well as their action on the eigenstates of the quantum harmonic oscillator $|n\rangle$ with $n \in \mathbb{N}_0$ are given by

$$\begin{aligned} [\hat{a}, \hat{a}^\dagger] &= \hat{1}, \\ \hat{a}|n\rangle &= \sqrt{n}|n-1\rangle, \\ \hat{a}^\dagger|n\rangle &= \sqrt{n+1}|n+1\rangle. \end{aligned} \tag{2.7}$$

The Fock states $|n\rangle$ are labeled by the number of bosons (e.g. photons) in the system, and the ladder operators incrementally change this number. Since $\hat{a}$ and $\hat{a}^\dagger$ appear quadratically in Eq. 2.6, quantum mechanical parametric driving can be understood as the creation of photon pairs.

2.2 Lindblad master equation

A physical system at a fixed point in time is fully described by its density operator $\hat{\rho}$. It stands for an ensemble of states $|\psi\rangle_k \in \mathcal{H}$, where $\mathcal{H}$ is the appropriate Hilbert space of the system and the index k labels all possibly occurring states. If each state $|\psi\rangle_k$ is realized with a probability p_k, the density operator can be written as

$$\hat{\rho} = \sum_k p_k |\psi_k\rangle\langle\psi_k|. \tag{2.8}$$

Independently of any specific basis representation, a density operator has to fulfill three conditions:

$$\begin{aligned} &1.)\ \mathrm{tr}\,(\hat{\rho}) = 1 && \text{Normalization} \\ &2.)\ \hat{\rho}^\dagger = \hat{\rho} && \text{Hermiticity} \\ &3.)\ \langle\psi|\hat{\rho}|\psi\rangle \geq 0\ \forall\psi \in \mathcal{H} && \text{Positive semi-definiteness} \end{aligned} \tag{2.9}$$

The expectation value of an arbitrary linear operator $\hat{O} \in \mathcal{O}$ [1] for a system with density operator $\hat{\rho}$ is calculated as

$$\langle\hat{O}\rangle = \mathrm{tr}\,(\hat{O}\hat{\rho}), \tag{2.10}$$

which is also not dependent on the choice of basis. If the full system's Hamiltonian and an initial condition are known, the time evolution of the density operator is found by solving the von-Neumann equation

$$\dot{\hat{\rho}}(t) = -i[\hat{H}, \hat{\rho}(t)]. \tag{2.11}$$

The trace of $\dot{\hat{\rho}}$ vanishes due to the cyclic property of the trace, so the equation preserves the normalization of the density operator. Likewise, the other two properties from Eq. 2.9 are preserved as well. A function mapping $\hat{\rho}(0)$ onto its time-evolved version $\hat{\rho}(t)$ while preserving positive semi-definiteness is called a positive map. The von-Neumann equation describes unitary time evolution and follows from the Schrödinger equation.

Oftentimes, however, it is convenient to divide a system with Hilbert space $\mathcal{H}_{tot}$ into two subsystems, i.e. $\mathcal{H}_{tot} = \mathcal{H}_1 \otimes \mathcal{H}_2$. If one is only interested in the state of the subsystem 1, a partial trace over all degrees of freedom of Hilbert space 2 yields the reduced density operator $\hat{\rho}_1 = \mathrm{tr}_2\,(\hat{\rho})$. Knowing it is sufficient for calculating expectation values of operators acting only on the first subspace. In the regarded case, the relevant subsystem is that of the parametric oscillator with Hilbert space $\mathcal{H}$. The second subsystem is a thermalized environment which can exchange photons with the former. Since only the Hamiltonian of the oscillator is known but there is an interaction between the subsystems, the Hamiltonian is not the generator of time evolution on $\mathcal{H}$. Instead, the dynamics are described by the **Lindblad master equation** (Ref. [4]). In this particular case, it takes the form

$$\dot{\hat{\rho}}(t) = -i[\hat{H}, \hat{\rho}(t)] + \gamma(\bar{n}+1)D[\hat{a}]\hat{\rho}(t) + \gamma\bar{n}D[\hat{a}^\dagger]\hat{\rho}(t), \tag{2.12}$$

which consists of the von-Neumann equation and two additional terms containing the interaction rate γ with the environment. Comparing this to the classical Eq. 2.4 shows that the interaction takes the role of the dissipative damping terms. The dissipator defined by

$$D[\hat{a}]\hat{\rho} = \hat{a}\hat{\rho}\hat{a}^\dagger - \frac{1}{2}\{\hat{a}^\dagger\hat{a}, \hat{\rho}\} \tag{2.13}$$

[1] $\mathcal{O}$ denotes the set of linear maps $\mathcal{H} \to \mathcal{H}$.

is a so called **superoperator**, which is a map $\mathcal{O} \to \mathcal{O}$. We omit the circumflex to distinguish superoperators from normal operators. Indeed, all of Eq. 2.12 can be expressed as a superoperator $\mathcal{L}$ acting on the density operator as

$$\dot{\hat{\rho}}(t) = \mathcal{L}\hat{\rho}(t). \tag{2.14}$$

$\mathcal{L}$ is called the Lindbladian or Liouvillian. $D[\hat{a}]$ is a jump (super-)operator which lowers the occupation number of each ket and bra in the density matrix (c.f Eq. 2.7). Conversely, $D[\hat{a}^\dagger]$ increases it. $\bar{n}$ is the Bose-Einstein occupation given by

$$\bar{n} = \frac{1}{e^{\beta\omega_0} - 1} \tag{2.15}$$

and quantifies the mean number of thermal photons of frequency ω_0 at fixed inverse temperature β. Therefore, the term proportional to $D[\hat{a}]$ in Eq. 2.12 contains a contribution from stimulated and spontaneous photon emission, while the counterpart $D[\hat{a}^\dagger]$ describes absorption of photons. Overall, we can think of the system as a resonator with a parametrically driven oscillator which interacts with a thermalized bath through the exchange of photons.
The anticommutator in the dissipator is needed so that $\mathrm{tr}\,(D[\hat{a}]\hat{\rho}) = 0$. Therefore, the important trace-preserving property of the von-Neumann equation also applies to the Lindblad equation in the form of

$$\mathrm{tr}\,(\mathcal{L}\hat{\rho}(t)) = 0, \tag{2.16}$$

which means that a density matrix undergoing Lindbladian time evolution will always retain its normalization. Additionally to the preservation of Hermiticity [2], it can also be shown that $\mathcal{L}$ is completely positive (CP), which means that the time evolution is a positive map for reduced density matrices in all possible subsystems (c.f. Ref. [5]).
The most important difference between Eq. 2.11 and Eq. 2.12 is that the Lindblad equation describes non-unitary time evolution. One consequence of this is that there does not exist a real Heisenberg picture in which the operators are time-dependent, because its justification stems from the unitary equivalence to the Schrödinger picture. Regardless, it is possible to find a similar formalism (with some caveats), as we will show in Ch. 4.

[2] $\mathcal{L}\hat{\rho}$ is Hermitian. $\mathcal{L}$ itself as a superoperator, however, is not.

Chapter 3

Emission of radiation

3.1 Photon current characterization

This chapter deals with the radiation emitted by the system which can be measured by a detector. The relevant observable is the photon current operator. We first define the operator $\hat{\mathcal{I}} = \gamma \hat{a}^\dagger \hat{a}$. When looking at the expectation value of $\hat{\mathcal{I}}$ given by

$$\langle \hat{\mathcal{I}} \rangle = \gamma \operatorname{tr}(\hat{a}^\dagger \hat{a} \hat{\rho}) = \gamma \operatorname{tr}(\hat{a} \hat{\rho} \hat{a}^\dagger), \tag{3.1}$$

it becomes apparent that it is equivalent to use the occupation number operator or to apply the annihilation operator from the left and the creation operator from the right. The second arrangement measures the photon current leaving the resonator [1]. Only the outgoing photons can be counted because a measurement of the occupation number collapses the ensemble into a single Fock state. Thus, the photon current operator is given by $\hat{\mathcal{I}}$, in the sense of the second arrangement. While the operator ordering does not make a difference in this case, the two arrangements are not generally equivalent. We will introduce the notation to distinguish them when the correlation of photon currents at different times is considered in Ch. 4.
The prefactor of the dissipator contains the Bose-Einstein occupation $\bar{n}$. It is absent in $\hat{\mathcal{I}}$ because the detector in the regarded model is located at an effective temperature $T = 0$ and does not measure thermal photons from anywhere but the resonator. The damping rate γ introduces a characteristic time scale for photon emission events. And the mean number of emitted photons per event is determined by the probability distribution contained in the density operator, which evolves according to Eq. 2.12.

The differential equation for calculating the expectation value of an arbitrary, time-independent operator $\hat{O} \in \mathcal{O}$ as a function of time is given by

$$\begin{aligned} \langle \dot{\hat{O}} \rangle(t) &= \operatorname{tr}(\hat{O} \dot{\hat{\rho}}(t)) \\ &= i \left\langle [\hat{H}, \hat{O}] \right\rangle + \gamma \bar{n} \left\langle [[\hat{a}, \hat{O}], \hat{a}^\dagger] \right\rangle + \gamma \left\langle \frac{1}{2} [\hat{O}, \hat{a}^\dagger \hat{a}] + [\hat{a}^\dagger, \hat{O}] \hat{a} \right\rangle, \end{aligned} \tag{3.2}$$

[1] C.f. the same structure appearing in the dissipator in Eq. 2.13.

where the cyclic property of the trace, the commutation relation in Eq. 2.7, and the Lindblad equation have been used. This leads to a closed system of first order ODEs including the occupation number operator, which we write in the form

$$\frac{d}{dt}\begin{pmatrix}\langle\hat{a}^\dagger\hat{a}\rangle(t)\\ \langle\hat{a}^2\rangle(t)\\ \langle\hat{a}^{\dagger 2}\rangle(t)\\ 1\end{pmatrix} = \begin{pmatrix}-\gamma & \frac{\epsilon}{2} & \frac{\epsilon}{2} & \gamma\bar{n}\\ \epsilon & -\gamma - i\Delta & 0 & \frac{\epsilon}{2}\\ \epsilon & 0 & -\gamma + i\Delta & \frac{\epsilon}{2}\\ 0 & 0 & 0 & 0\end{pmatrix}\begin{pmatrix}\langle\hat{a}^\dagger\hat{a}\rangle(t)\\ \langle\hat{a}^2\rangle(t)\\ \langle\hat{a}^{\dagger 2}\rangle(t)\\ 1\end{pmatrix}. \tag{3.3}$$

The fourth subspace has been added to incorporate the inhomogeneity into the matrix. Thus, results from the theory of homogeneous systems can be used (Ref. [6]). A homogeneous linear system is asymptotically stable at its critical point (the point where the derivative is equal to 0) if all eigenvalues have a negative real part with the exception of the eigenvalue 0 which has to have an algebraic multiplicity equal to its geometric multiplicity. Physically, asymptotic stability means that the system will reach a steady state for $\gamma t \to \infty$ for any initial condition. Then, the density matrix does not change anymore which corresponds to a stationary probability distribution. The eigenvalues of the matrix in Eq. 3.3 are $\lambda_1 = -\gamma$, $\lambda_2 = -\gamma - \sqrt{\epsilon^2 - \Delta^2}$, $\lambda_3 = -\gamma + \sqrt{\epsilon^2 - \Delta^2}$ as well as the steady state characterized by the eigenvalue 0. The restriction for asymptotic stability arises from λ_3. If ϵ is greater than or equal to the **threshold driving strength**

$$\epsilon_{\text{thr}} = \sqrt{\Delta^2 + \gamma^2}, \tag{3.4}$$

one of the two conditions for asymptotic stability is violated and the system will not reach a steady state. This classically corresponds to the amplitude growing indefinitely. Without detuning, this instability occurs right when the driving exceeds the damping rate. With detuned driving, the threshold is shifted toward higher ϵ because non-resonant driving - speaking in classical terms - is less effective in increasing the oscillation amplitude. The same threshold is also valid for the classical case, because the eigenvalues of the matrix in Eq. 2.3 are the same as λ_2 and λ_3 apart from a prefactor.
If $\Delta = \epsilon \neq 0$, the matrix is not diagonalizable and the expectation value does not evolve purely exponentially anymore. Since this case is a very specific choice of parameters and is of no particular interest, we exclude it.
For $\epsilon = 0$, the 3×3 subspace of Eq. 3.3 is diagonal. The differential equations are not coupled anymore. This case generally has to be regarded separately because the calculation of the eigenvectors otherwise involves dividing by ϵ.
Another noteworthy fact is that the eigenvalues are all real if $\epsilon \geq \Delta$, and if that is not the case, they appear in complex conjugate pairs.

By finding the kernel of the matrix, we acquire the photon current in the steady state (denoted by the subscript s), which is given by

$$\langle\hat{\mathcal{I}}\rangle_s = \gamma\left(\frac{\bar{n}(\Delta^2 + \gamma^2) + \frac{\epsilon^2}{2}}{\Delta^2 + \gamma^2 - \epsilon^2}\right). \tag{3.5}$$

This result differs from the classical parametric oscillator. Both amplitudes x_1 and x_2 in the classical differential equation will eventually reach 0 below threshold because Eq. 2.3 is inherently homogeneous. In contrast, the photon current approaches a non-zero value.

Stronger driving results in a considerably higher equilibrium photon rate, diverging at $\epsilon \to \epsilon_{\text{thr}}$. On the other hand, it decreases as Δ grows. This is because the driving is off-resonant which hampers its efficiency, as mentioned above.
Also, $\langle\hat{\mathcal{I}}\rangle_s$ depends linearly on the Bose-Einstein occupation. Without driving, the resonator is in thermal equilibrium with the environment, which is expressed by $\langle\hat{a}^\dagger\hat{a}\rangle = \bar{n}$. If the driving strength is increased, the thermal photons do not only leave the resonator directly but can also create even higher excitations than the driving alone does, further increasing the radiation emission. Therefore, the slope of $\langle\hat{\mathcal{I}}\rangle_s$ as a function of $\bar{n}$ increases as $\epsilon \to \epsilon_{\text{thr}}$.
The influence of the damping rate on $\langle\hat{\mathcal{I}}\rangle_s$ depends on whether or not thermal photons are present. At $\bar{n} = 0$, the photon current decreases with γ because a higher interaction rate shifts the probability distribution in the density operator toward lower occupation numbers. If the temperature is not 0, the thermal photons will outweigh that effect at some point and the current will begin to increase again with γ.

The complete time evolution of the three expectation values in Eq. 3.3 can now be easily obtained by finding the other three eigenvectors $\boldsymbol{v_1}$, ..., $\boldsymbol{v_3}$ corresponding to the non-zero eigenvalues and constructing a linear combination $\boldsymbol{v_s} + \sum_{i=1}^{3} A_i e^{\lambda_i t}\boldsymbol{v_i}$ where $\boldsymbol{v_s}$ contains the steady state values. We choose the vacuum state $\hat{\rho}_0 = |0\rangle\langle 0|$ as the initial condition and fix the constants A_i accordingly.

The solution for $\epsilon = 0$ is given by

$$\langle\hat{\mathcal{I}}\rangle(t) = \langle\hat{\mathcal{I}}\rangle_s(1 - e^{-\gamma t}) \tag{3.6}$$

and describes the process in which the system thermalizes with the environment through the exchange of photons. The current increases with a characteristic time of γ^{-1} until an equilibrium at $\langle\hat{\mathcal{I}}\rangle_s = \gamma\bar{n}$ is reached.

For $\Delta = 0$, we obtain

$$\langle\hat{\mathcal{I}}\rangle(t) = \langle\hat{\mathcal{I}}\rangle_s - \frac{\gamma}{2}\left(\frac{\bar{n}\gamma - \frac{\epsilon}{2}}{\gamma + \epsilon}\cdot e^{-(\gamma+\epsilon)t} + \frac{\bar{n}\gamma + \frac{\epsilon}{2}}{\gamma - \epsilon}\cdot e^{-(\gamma-\epsilon)t}\right). \tag{3.7}$$

Unlike the previous case, there are two exponential functions decaying with characteristic times $(\gamma+\epsilon)^{-1}$ and $(\gamma-\epsilon)^{-1}$. The second, slowly decaying mode dictates the time scale τ_* at which the system approaches the steady state. So additionally to $\langle\hat{\mathcal{I}}\rangle_s$, the limit $\epsilon \to \epsilon_{\text{thr}}$ also causes τ_* to diverge.

In order to verify the results, we explain the numerical approach to solving the Lindblad equation. The method is also important when nonlinearities are

included and an analytical solution is not obtainable.
The first step is to determine a matrix representation of the occurring operators $\hat{a}$, $\hat{a}^\dagger$ and $\hat{\rho}$. We use the Fock basis for now, because it is the natural basis when ladder operators are involved. The bosonic Hilbert space is infinite dimensional, but numerical calculation requires turning the operators into matrices of finite size. For the Fock states, this can be done by only allowing states $|n\rangle$ with $n \leq n_{\max}$. The idea behind this cutoff is that the probability for a much higher occupation than $\langle \hat{a}^\dagger \hat{a} \rangle_s$ is very low, and therefore the matrix elements in the corresponding subspaces tend to 0. Depending on which operations are performed on the density matrix before taking the trace, the contribution from these subspaces can be neglected without changing the result substantially. The caveat is that applying operators to the density matrix shifts the weight of distribution away from $\langle \hat{a}^\dagger \hat{a} \rangle_s$ or may increase its variance. This means that $n_{\max}$ needs to be increased dynamically until further changes do not influence the results of the calculation up to a desired accuracy.
In this way, the ladder operators as well as the density operator can be represented by matrices, e.g.

$$\hat{a} \doteq \begin{pmatrix} 0 & \sqrt{1} & 0 & \cdots & 0 & 0 \\ 0 & 0 & \sqrt{2} & \cdots & 0 & 0 \\ 0 & 0 & 0 & \cdots & 0 & 0 \\ \vdots & \vdots & \vdots & \ddots & \vdots & \vdots \\ 0 & 0 & 0 & \cdots & 0 & \sqrt{n_{\max}} \\ 0 & 0 & 0 & \cdots & 0 & 0 \end{pmatrix}. \tag{3.8}$$

For the simulation, we use the forward Euler method, in which the derivative $\dot{\hat{\rho}}$ in Eq. 2.12 is estimated as a simple quotient $\frac{\Delta \hat{\rho}}{\Delta t}$. The time step Δt has to be chosen sufficiently small for numerical accuracy. If $\hat{\rho}_i$ is the density matrix at time t, the update to $\hat{\rho}_{i+1}$ at time $t + \Delta t$ is then calculated as

$$\hat{\rho}_{i+1} = \hat{\rho}_i + (\mathcal{L}\hat{\rho}_i)\Delta t. \tag{3.9}$$

The trace preserving property of the analytical Lindblad equation (Eq. 2.16) does not apply to the numerical approximation. It is therefore important to normalize the matrix after each simulation step. The ladder operators are represented by sparse matrices in the Fock basis. This can be used to significantly decrease the simulation time.

With the described method, the analytical results can be validated by comparing them to the simulation. Fig. 3.1a shows the time evolution of the photon current during the approach of the steady state. The parameters have all been set to nonzero values to confirm that the analytical solution matches the simulation in a general case. The exponential decay toward the steady state current is visible. It is in generally a linear combination of all three modes. The behavior of the steady state photon current can be seen in Fig. 3.1b for varying detuning. The shifting threshold with increasing values of Δ according to Eq. 3.4 is verified as well as the decrease of $\langle \hat{\mathcal{I}} \rangle_s$ for fixed driving strength when the driving gets more detuned. Fig. 3.1c shows what happens when $\bar{n}$ is varied. The

direct proportionality of the photon current on the Bose-Einstein occupation becomes apparent due to the equal spacing between the graphs.

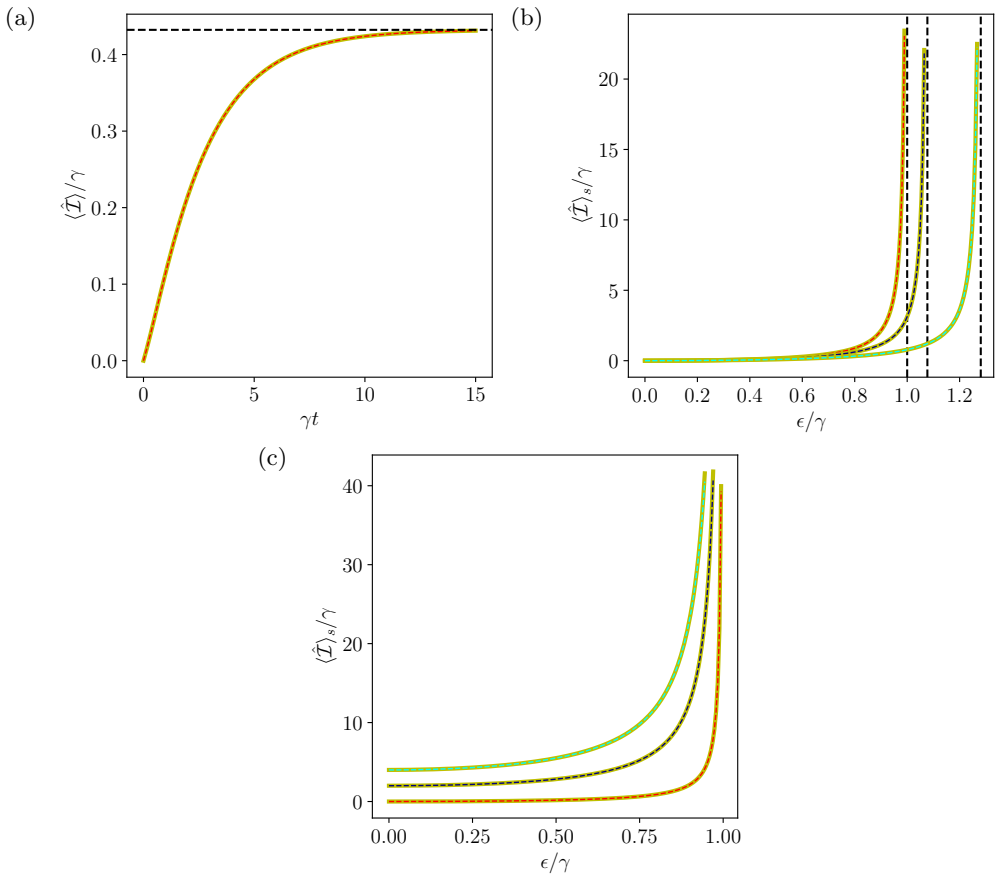

Figure 3.1: Comparison of numerical and analytical solutions for the expectation value of the photon current. The analytical solutions are represented by yellow lines in all subfigures. (a) Approach of the steady state, marked by the dashed black line. The values of $\epsilon = 0.6\gamma$, $\Delta = 0.1\gamma$ and $\bar{n} = 0.1$ have been chosen to show that the analytical solution and the simulation (dashed red) coincide in a general case. (b) Steady state photon current depending on ϵ for $\bar{n} = 0$. The detuning takes values of $\Delta = 0$ (dashed red), $\Delta = 0.4\gamma$ (dashed blue) and $\Delta = 0.8\gamma$ (dashed cyan). The threshold (dashed black) shifts according to Eq. 3.4. (c) Steady state photon current without detuning depending on ϵ for $\bar{n} = 0$ (dashed red), $\bar{n} = 2$ (dashed blue) and $\bar{n} = 4$ (dashed cyan). The limit $\epsilon \ll \gamma$ shows that $\langle \hat{\mathcal{I}} \rangle_s \to \gamma \bar{n}$.

3.2 Stabilization above threshold

From classical mechanics, we know that unstable systems can be stabilized by adding a term of higher order to the potential. An example of this is that the potential $V(x) = -x^2$ always causes the kinetic energy of a mass placed anywhere but at the metastable point $x = 0$ to increase indefinitely. An additional term proportional to x^4 allows for bounded solutions.
The same can be done to stabilize the parametric oscillator for $\epsilon \geq \epsilon_{\mathrm{thr}}$. To this end, a nonlinear potential term is introduced into the Hamiltonian which can be realized in a voltage-biased Josephson junction. It is given by

$$\hat{V} = i\alpha\epsilon(\hat{a}^\dagger\hat{a}^3 - \hat{a}^{\dagger 3}\hat{a}), \tag{3.10}$$

where $\alpha \ll 1$ is a dimensionless coupling constant (Ref. [3]).
The fourth-order terms make it impossible to calculate the photon current analytically because the derivatives always couple to terms of higher order. This does not yield a closed system like the one in Eq. 3.3. Instead, we rely on the numerical method to simulate the dynamics.

Fig. 3.2a shows the time evolution of the photon current for different coupling constants above threshold. The system does reach a steady state eventually, therefore the potential in Eq. 3.10 is suited for stabilization of the parametric oscillator. Consequently, the time scale τ_* also remains finite. However, the figure shows that it is greatly increased compared to driving well below threshold (c.f. Fig. 3.1a). This reveals the necessity to look for more efficient ways of obtaining the steady state density matrix, which will be done in the next chapter. τ_* is greater for smaller values of α, because a weakly coupled stabilizing potential is not as effective in quickly stopping the system from diverging. The shape of the graph is altered when the anharmonicity is introduced. Instead of a strictly exponential approach of the steady state, the slope of the photon current starts at a value close to 0 and the curve has an inflection point. This property is generally true, also below threshold.

The steady state photon current as a function of the driving strength is depicted in Fig. 3.2b for different values of α. $\langle\hat{\mathcal{I}}\rangle_s$ has an inflection point above threshold. While its values remain below 5γ in the regime $\epsilon < \gamma$, it reaches about 5 times its threshold value at $\epsilon = 2\gamma$. The values of α have been chosen so that α^{-1} increases in constant steps of 50 between the curves. Close to the highest depicted driving strength of $\epsilon = 2\gamma$, we can ascertain that the steady state photon current grows approximately linearly with α^{-1}. This means, equivalently, that the singularity at $\alpha \to 0^+$ is approached with hyperbolic growth for strong driving far above threshold.

Fig. 3.2c depicts the time evolution of the photon current for different values of ϵ when all other parameters remain constant. The important insight gained through this graph is that τ_* does not increase monotonously with ϵ. It rather has a maximum somewhere between $\epsilon = 1.1\gamma$ and $\epsilon = 1.3\gamma$, after which the steady state is reached more quickly again.

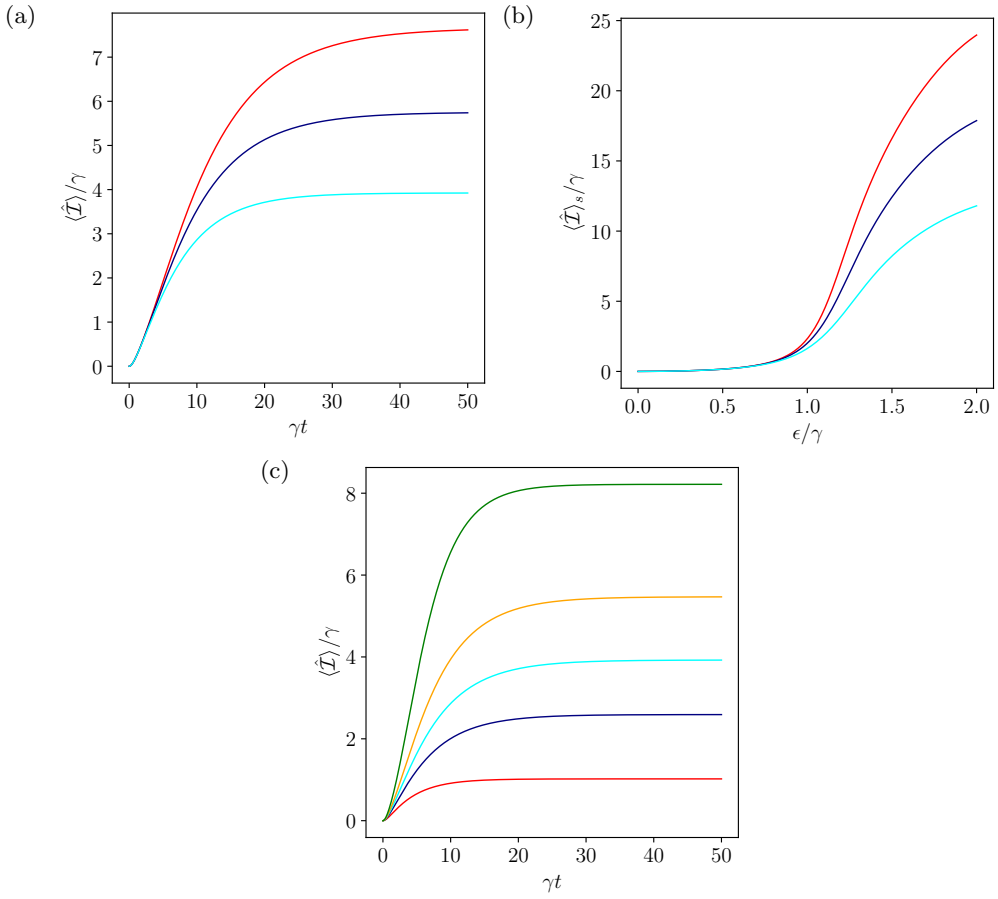

Figure 3.2: Numerical simulation of the photon current with the stabilizing potential. (a) Approach of the steady state at $\epsilon = 1.2\gamma$ and $\bar{n} = \Delta = 0$. The values of the coupling constant have been chosen as $\alpha = 0.005$ (red), $\alpha = 0.00\overline{6}$ (blue) and $\alpha = 0.01$ (cyan) so that α^{-1} is equidistant. The characteristic time scale τ_* increases with α and is higher than below threshold. Nonetheless, a steady state is reached eventually. (b) Steady state photon current depending on ϵ, now in the range from 0 to 2γ. The color coding is the same as in (a). Above threshold, $\langle \hat{\mathcal{I}} \rangle_s$ increases significantly compared to below. (c) Approach of the steady state at $\bar{n} = \Delta = 0$ and $\alpha = 0.01$ for $\epsilon = 0.9\gamma$ (red), $\epsilon = 1.1\gamma$ (blue), $\epsilon = 1.2\gamma$ (cyan), $\epsilon = 1.3\gamma$ (orange) and $\epsilon = 1.5\gamma$ (green). Out of the depicted curves, the cyan one takes the longest time to reach an equilibrium. Therefore, τ_* is not monotonous in ϵ.

Chapter 4

Second-order coherence

4.1 Correlation of photon emission

For classical light with intensity $\bar{I}(t)$ at time t[1], the **second-order (temporal) coherence** is defined by

$$g^{(2)}(\tau) = \frac{\langle \bar{I}(t)\bar{I}(t+\tau)\rangle}{\bar{I}^2}, \tag{4.1}$$

where $\bar{I}$ without a time argument stands for the long-time average of $\bar{I}(t)$ and the brackets denote an ensemble average. The coherence is a normalized measure for the correlation of the light's intensities at two points separated in time by the delay τ. We implicitly assume a light source with statistical properties that are not time-dependent, i.e. stationary. This explains why $g^{(2)}(\tau)$ does not depend on t, which can be set to 0. Because of the single argument of $g^{(2)}$ and since the intensities can be freely commuted, setting $t' = t - \tau$ shows that the function is even, $g^{(2)}(-\tau) = g^{(2)}(\tau)$.

We now want to consider the quantum mechanical analogue. Classical intensities are proportional to photon currents because all emitted photons have the same frequency ω_0. We assume that the system is in its steady state at $t = 0$. The second-order coherence is therefore expressed as

$$g^{(2)}(\tau) = \frac{\mathrm{tr}\left(\hat{a}(\tau)\hat{a}(0)\hat{\rho}_s\hat{a}^\dagger(0)\hat{a}^\dagger(\tau)\right)}{\mathrm{tr}\left(\hat{a}\hat{\rho}_s\hat{a}^\dagger\right)^2}. \tag{4.2}$$

Note that the order of the operators to the left and right of the density operator is important, unlike in Eq. 3.1. This is called normal ordering and can be denoted by colons as

$$g^{(2)}(\tau) = \frac{\langle :\hat{\mathcal{I}}(\tau)\hat{\mathcal{I}}(0):\rangle_s}{\langle\hat{\mathcal{I}}\rangle_s^2}. \tag{4.3}$$

The time argument of the operators is suggestive of the method that will be used to calculate the coherence, but Eq. 4.2 can be interpreted to mean that the

[1]The bar implies that the intensity is averaged over one or a few oscillation cycles of the light around time t.

system first interacts with the environment at time 0, when the outgoing photon rate is measured. Due to the interaction, the density operator changes and is not in the steady state anymore. The system undergoes Lindblad time evolution for a time τ, and then it is determined how the photon rate is correlated to the one previously measured.
Following the classical case, the quantum mechanical coherence is defined to be an even function. The behavior for $\tau \to \infty$ can be extracted from Eq. 4.2: Applying $\hat{a}(0)$ and $\hat{a}^\dagger(0)$ to $\hat{\rho}_s$ and canceling one factor in the denominator yields a density operator with trace 1 that will eventually reach the steady state again. Therefore, the coherence will approach 1 in the long time-delay limit, independently of the system.
Light with $g^{(2)}(\tau) \equiv 1$ is called second-order coherent. In this case, the photon currents are independent of the time passed since the last measurement [2]. This and the fact that the mean photon current is constant means that the system exhibits Poissonian counting statistics as found, e.g., in lasers.
For the classical case in Eq. 4.1, the Cauchy-Schwarz inequality implies that $g^{(2)}(0) \geq g^{(2)}(\tau)$ for all $\tau \in \mathbb{R}$. Furthermore, $g^{(2)}(0) \geq 1$ because the variance of $\bar{I}(t)$ is greater than 0. This generally does not hold true when the intensities are replaced by quantum mechanical operators that do not commute, as in Eq. 4.2. Compare Ref. [7] for a more detailed discussion of the coherence and proofs of the general properties.

4.2 Coherence for the parametric oscillator

We first want to look at the linear problem and find an analytical expression for the coherence. While there are multiple ways to do this, we introduce a method which resembles the Heisenberg picture in unitary time evolution. To this end, a superoperator $\mathcal{L}'$ can be found such that for every operator $\hat{O} \in \mathcal{O}$ and an arbitrary density matrix $\hat{\rho}$, the relation

$$\mathrm{tr}\left(\hat{O}(\mathcal{L}\hat{\rho})\right) = \mathrm{tr}\left((\mathcal{L}'\hat{O})\hat{\rho}\right) \tag{4.4}$$

holds true. The exponential function for (super-)operators is defined as a power series. Repeated application of Eq. 4.4 in the terms of the series yields that $e^{\mathcal{L}'t}$ can be applied to the operator instead of $e^{\mathcal{L}t}$ to the density matrix without changing the expectation value. Thus, a time-dependent operator can be defined, which obeys the differential equation

$$\dot{\hat{O}}(t) = \mathcal{L}'\hat{O}(t). \tag{4.5}$$

$\mathcal{L}'$ is obtained through cyclic permutation of the terms within the trace in Eq. 4.4. This results in the expression

$$\dot{\hat{O}}(t) = i[\hat{H}, \hat{O}(t)] + \left(\gamma(\bar{n}+1)D[\hat{a}^\dagger] + \gamma\bar{n}D[\hat{a}] + \gamma\right)\hat{O}(t). \tag{4.6}$$

An important difference between the Heisenberg picture and this time evolution of operators is that they do not, in general, evolve independently of one another.

[2] More formally, the covariance between $\hat{\mathcal{I}}(\tau)$ and $\hat{\mathcal{I}}(0)$ is 0.

A product of two operators $\hat{O}_1$ and $\hat{O}_2$ under unitary time evolution can be written as $(\hat{O}_1\hat{O}_2)(t) = e^{i\hat{H}t}\hat{O}_1\hat{O}_2e^{-i\hat{H}t} = e^{i\hat{H}t}\hat{O}_1e^{-i\hat{H}t}e^{i\hat{H}t}\hat{O}_2e^{-i\hat{H}t} = \hat{O}_1(t)\hat{O}_2(t)$. Inserting a 1 like this is not possible if the generator of time evolution is not Hermitian and it is necessary to evolve the product operator as a whole.

Eq. 4.2 shows that the time-dependent operator $(\hat{a}^\dagger\hat{a})(t)$ is required to calculate the coherence. Knowing the results for the expectation values from the previous chapter, it is prudent to assume that only operators of the same order and the identity operator are mixed as $\hat{a}^\dagger\hat{a}$ changes over time. With the ansatz

$$(\hat{a}^\dagger\hat{a})(t) = f(t)\hat{a}^\dagger\hat{a} + g(t)\hat{a}^2 + h(t)\hat{a}^{\dagger 2} + l(t)\hat{1} \tag{4.7}$$

and the initial condition $(\hat{a}^\dagger\hat{a})(0) = \hat{a}^\dagger\hat{a}$, we retain a system of differential equations for the functions f, g, h and l. It is given by

$$\frac{d}{dt}\begin{pmatrix} f(t) \\ g(t) \\ h(t) \\ l(t) \end{pmatrix} = \begin{pmatrix} -\gamma & \epsilon & \epsilon & 0 \\ \frac{\epsilon}{2} & -\gamma - i\Delta & 0 & 0 \\ \frac{\epsilon}{2} & 0 & -\gamma + i\Delta & 0 \\ \gamma\bar{n} & \frac{\epsilon}{2} & \frac{\epsilon}{2} & 0 \end{pmatrix}\begin{pmatrix} f(t) \\ g(t) \\ h(t) \\ l(t) \end{pmatrix}, \tag{4.8}$$

which is the adjoint of the matrix from Eq. 3.3. This means that it has the same eigenvalues because they appear in complex conjugate pairs. It is no surprise that the systems are almost identical because the time evolution of the operator can also be used to calculate the photon current and vice versa - it is the same problem from a different perspective.
The general solution is found by diagonalizing the 3×3 subspace for f, g and h and then integrating to get l. When $(\hat{a}^\dagger\hat{a})(t)$ is known, the coherence is calculated as

$$g^{(2)}(\tau) = \frac{1}{\langle\hat{a}^\dagger\hat{a}\rangle_s^2}\left[f(\tau)\langle\hat{a}^{\dagger 2}\hat{a}^2\rangle_s + g(\tau)\langle\hat{a}^\dagger\hat{a}^3\rangle_s + h(\tau)\langle\hat{a}^{\dagger 3}\hat{a}\rangle_s + l(\tau)\langle\hat{a}^\dagger\hat{a}\rangle_s\right]. \tag{4.9}$$

The fourth-order expectation values in the steady state are determined analogously to $\langle\hat{\mathcal{I}}\rangle_s$ in chapter 2 with Eq. 3.2. It is evident that obtaining the coherence in this way involves a lot of calculations. A much more effective method will be provided in Ch. 6.

Since the eigenvalues of Eq. 3.3 and Eq. 4.8 are identical, the coherence has the same exponentially decaying modes as the photon current. This means that the characteristic time for the approach of the steady state τ_* is also the typical correlation time between photon emissions.

For $\epsilon = 0$, the coherence takes the form

$$g^{(2)}(\tau) = 1 + e^{-\gamma\tau}, \tag{4.10}$$

which is completely independent of temperature and detuning. This is similar to the behavior found for the photon current. However, the global prefactor given by the steady state photon current did depend on the temperature

whereas the coherence always starts off at a value of 2. It decays exponentially with a correlation time of γ^{-1}. The emitted light is not second-order coherent, which means that thermal photons (the only ones present in this special case) are correlated with each other.

In the case of $\Delta = 0$ with nonzero driving, we obtain

$$g^{(2)}(\tau) = 1 + \frac{(\epsilon - 2\gamma\bar{n})^2(\gamma - \epsilon)^2}{2(\epsilon^2 + 2\gamma^2\bar{n})^2} e^{-(\gamma+\epsilon)\tau} + \frac{(\epsilon + 2\gamma\bar{n})^2(\gamma + \epsilon)^2}{2(\epsilon^2 + 2\gamma^2\bar{n})^2} e^{-(\gamma-\epsilon)\tau}. \quad (4.11)$$

Both modes contribute differently to the coherence. The starting value of the function is given by

$$g^{(2)}(0) = 2 + \left(\frac{\gamma\epsilon(2\bar{n} + 1)}{2\gamma^2\bar{n} + \epsilon^2} \right)^2 \quad (4.12)$$

and is always greater than or equal to 2. If $\bar{n} \neq 0$, it approaches 2 in the limit $\epsilon \to 0$, as expected from Eq. 4.10. However, if $\bar{n} = 0$, $g^{(2)}(0)$ diverges when taking the limit. This is an example of the fact that $\epsilon \to 0$ generally does not commute with the vanishing of other parameters, as mentioned in Ch. 3. The discrepancy can be explained physically. In the zero temperature limit, the correlation between photons stems purely from the driving process. We remember the interpretation of the driving term in Eq. 2.6 as creating pairs of photons, which are necessarily correlated with each other. For small but nonzero driving, the probability of two measured photons in short succession belonging to the same creation event is very high. They are therefore almost certainly correlated. As the driving strength increases, more photon pairs are produced which reduces the likelihood of measuring photons from the same driving event.
If the temperature is increased, the thermal radiation destroys the certainty of correlation close to $\tau = 0$ for $\epsilon \to 0$. Only the contribution from the correlation of thermal photons remains. $g^{(2)}(0)$ has a peak for a certain driving strength [3]. It occurs when there are enough photons produced by driving for their correlation to be palpable despite the presence of thermal radiation.

The general solution of $g^{(2)}(\tau)$ confirms that the coherence always starts at a value > 1 and that $\tau = 0$ is the global maximum, just as in the regarded special cases. Right after a photon is emitted, there is a maximally increased probability of another emission. The property

$$\forall\tau : g^{(2)}(0) \geq g^{(2)}(\tau) \quad (4.13)$$

is called **photon bunching** and means that the photons tend to be detected in bunches, rather than individually (or independently of one another, like in coherent light). An example for the opposite would be the property of a single-photon source, which is conversely called **photon antibunching**. It is characterized by

$$\exists\delta > 0 : \forall\gamma\tau \in [-\delta, \delta] : g^{(2)}(0) \leq g^{(2)}(\tau). \quad (4.14)$$

[3] If $0 < n \leq 0.5$, the maximum value of $g^{(2)}(0)$ is equal to $2 + \frac{(2\bar{n}+1)^2}{8\bar{n}}$ at $\epsilon = \sqrt{2\bar{n}}\gamma$. If $\bar{n} > 0.5$, the maximum of $g^{(2)}(0) = 3$ is approached in the limit $\epsilon \to \gamma$.

The probability of detecting another photon is reduced right after an emission. As mentioned in the previous section, antibunching is not possible for classical light. And without the nonlinear term, it does not appear in the model of the parametrically driven oscillator.

In the following, we turn to the problem with the stabilizing potential. The numerical method introduced in the last chapter relies on simulating the dynamics of the Lindblad equation until the steady state is reached. We have seen in Fig. 3.2c that this can take a long time above threshold. Since the steady state is needed as the initial condition for the coherence, we introduce a method to obtain $\hat{\rho}_s$ immediately. To this end, the density operator $\hat{\rho} = \sum_{n,m=0}^{\infty} \rho_{n,m} |n\rangle\langle m|$ can be turned into a vector $|\hat{\rho}\rangle$ by identifying $|n\rangle\langle m|$ with the tensor product $|n\rangle \otimes |m\rangle$. Applying the ladder operators from the left or from the right can be distinguished in this formalism, because these operations are performed by distinct superoperators. The superoperators acting on the vectorized density matrix are defined as

$$\begin{aligned} a_+|\hat{\rho}\rangle &\coloneqq |\hat{a}\hat{\rho}\rangle = (\hat{a} \otimes \hat{1})|\hat{\rho}\rangle, \\ a_+^\dagger|\hat{\rho}\rangle &\coloneqq |\hat{a}^\dagger\hat{\rho}\rangle = (\hat{a}^\dagger \otimes \hat{1})|\hat{\rho}\rangle, \\ a_-|\hat{\rho}\rangle &\coloneqq |\hat{\rho}\hat{a}\rangle = (\hat{1} \otimes \hat{a}^\dagger)|\hat{\rho}\rangle, \\ a_-^\dagger|\hat{\rho}\rangle &\coloneqq |\hat{\rho}\hat{a}^\dagger\rangle = (\hat{1} \otimes \hat{a})|\hat{\rho}\rangle. \end{aligned} \tag{4.15}$$

Their matrix representation as well as technicalities concerning the right and left eigenbasis of $\mathcal{L}$ are discussed in App. A. The main result is that every superoperator, including the Liouvillian, is represented by a matrix acting from the left on the state $|\hat{\rho}\rangle$. This means that the Lindblad equation as given in Eq. 2.14 turns into a homogeneous system of first order ODEs solved by $|\hat{\rho}(t)\rangle = e^{\mathcal{L}t}|\hat{\rho}_0\rangle$. The steady state $|\hat{\rho}_s\rangle$ can thus be determined as the element of $\ker(\mathcal{L})$ with normalized trace. We will denote it with its eigenvalue as $|\tilde{0}\rangle$, where the tilde is used to distinguish the eigenvalue notation in the vectorized basis from the Fock states. Another important result from the appendix is that the trace is given by the left eigenvector $\langle\tilde{0}|$ of $\mathcal{L}$ with eigenvalue 0.

It must be noted that the dimension of the superoperator matrices is $n_{\max}^2 \times n_{\max}^2$ compared to $n_{\max} \times n_{\max}$ for the method explained in Ch. 3. However, the number of performed operations in each simulation step is reduced because it only involves applying $\mathcal{L}$ to the density matrix instead of multiple matrix multiplications with the ladder operators. Also, the utilization of sparse matrices means that the calculation time for each matrix multiplication does not increase quadratically with the dimension. Therefore, the simulation in this basis is not as inefficient as the matrix dimension might suggest.

In terms of the superoperators, the Liouvillian can be expressed as

$$\mathcal{L} = i(H_- - H_+) + \gamma(\bar{n} + 1)D[\hat{a}] + \gamma\bar{n}D[\hat{a}^\dagger] \tag{4.16}$$

with

$$\begin{aligned} H_+ &= \frac{\Delta}{2}a_+^\dagger a_+ + i\epsilon\left[\frac{1}{4}(a_+^{\dagger 2} - a_+^2) + \alpha(a_+^\dagger a_+^3 - a_+^{\dagger 3}a_+)\right], \\ H_- &= \frac{\Delta}{2}a_- a_-^\dagger + i\epsilon\left[\frac{1}{4}(a_-^{\dagger 2} - a_-^2) + \alpha(a_-^3 a_-^\dagger - a_- a_-^{\dagger 3})\right], \\ D[\hat{a}] &= a_+ a_-^\dagger - \frac{1}{2}(a_+^\dagger a_+ + a_- a_-^\dagger), \\ D[\hat{a}^\dagger] &= a_+^\dagger a_- - \frac{1}{2}(a_+ a_+^\dagger + a_-^\dagger a_-). \end{aligned} \tag{4.17}$$

The photon current operator with normal ordering takes the form $\mathcal{I} = \gamma a_+ a_-^\dagger$. Finally, the second-order coherence in this formalism is denoted by

$$g^{(2)}(\tau) = \frac{\langle\tilde{0}|a_+ a_-^\dagger e^{\mathcal{L}|\tau|} a_+ a_-^\dagger|\tilde{0}\rangle}{\langle\tilde{0}|a_+ a_-^\dagger|\tilde{0}\rangle^2}, \tag{4.18}$$

where the absolute value of τ is needed so that $g^{(2)}(\tau)$ is even.

We now have the tools to simulate the coherence function with the stabilizing potential. Fig. 4.1 shows $g^{(2)}(\tau)$ for different values of ϵ and fixed α. The regarded driving strengths have been selected because somewhere between $\epsilon = 1.5\gamma$ and $\epsilon = 1.6\gamma$, the photon current switches from being bunched to antibunched. This is the first occasion in the examined system in which the quantum nature of light creates results that cannot be explained classically. The nonlinear term alters the statistical properties of the emitted radiation and introduces the possibility of antibunched light above threshold. We will call the driving strength at which the radiation changes from bunched to antibunched the **critical driving strength** $\epsilon_{\mathbf{cr}}$. The cyan curve shows that $g^{(2)}(\tau)$ changes its shape close to ϵ_{cr}. It is also the first of the depicted graphs to meet the criterion from Eq. 4.14 for antibunching. The switch happens before $g^{(2)}(0)$ takes on values less than 1, as it has in the orange curve. However, between the blue, cyan and orange curves, the driving strength only changes by 0.03γ. Therefore, the alternative definition of the critical point as

$$g^{(2)}(0)|_{\epsilon=\epsilon_{\mathrm{cr}}} = 1 \tag{4.19}$$

is sensible and in good agreement with the previous one. This definition is often used in literature as the sole distinction between bunched and antibunched light (e.g. in Ref. [8]).

Based on Eq. 4.19, we can study the behavior of the critical point when one of the parameters at a time is varied. Fig. 4.2a shows the variation of the coupling constant at 0 temperature and detuning. The critical point increases only very slightly with α. Therefore, as long as the nonlinearity is present, the emission of antibunched light occurs around the same critical driving strength if the coupling constant is in the regarded interval. The behavior for $\alpha \to 0^+$ cannot be determined accurately because a smaller coupling constant increases the photon current and the required matrix size to obtain accurate results. The simulation

time grows significantly. For higher values of α, the slope of the curve decreases.

Fig. 4.2b depicts how increasing the temperature influences ϵ_{cr} at a fixed value of α and without detuning. For very small temperatures, a positive linear dependence on $\bar{n}$ can be observed. The change in ϵ_{cr} is significant compared to the behavior when α is varied. For higher temperatures, the slope increases and antibunching occurs at much higher values of ϵ. The general trend of ϵ_{cr} monotonously increasing with the temperature can be explained with the help of Eq. 4.10, where we saw that purely thermal radiation is bunched. Therefore, if the temperature is increased, the presence of thermal photons counteracts the effect of the nonlinear driving. The latter tries to turn the radiation into antibunched light if the driving strength is high enough, but the statistical properties of the thermal photons outweigh this up to much stronger driving.

In Fig. 4.2c, Δ is increased at zero temperature while α remains constant. Like in the other figures, the critical point also increases monotonously as the driving becomes more detuned. While the exact effect of detuning with the nonlinear potential is not easily interpreted, the tendency can be understood in that higher detuning causes the driving to become less effective. Therefore, a greater value of ϵ is needed so that the driving term with the nonlinearity produces antibunched light.

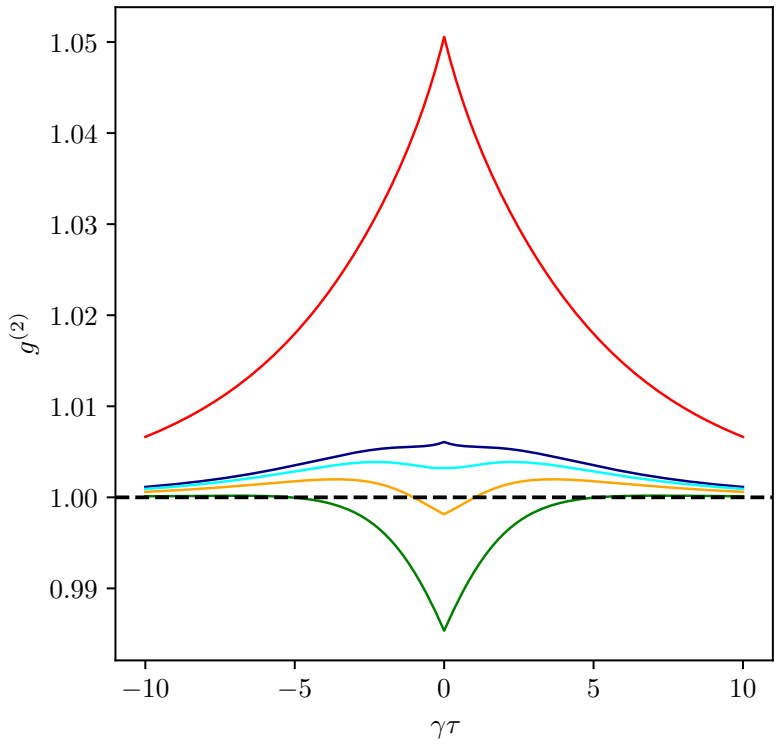

Figure 4.1: Simulated second-order coherence for different driving strengths with $\bar{n} = \Delta = 0$ and $\alpha = 0.01$. The values of $\epsilon = 1.4\gamma$ (red), $\epsilon = 1.5\gamma$ (blue), $\epsilon = 1.51\gamma$ (cyan), $\epsilon = 1.53\gamma$ (orange) and $\epsilon = 1.6\gamma$ (green) have been chosen because the emitted radiation changes from bunched to antibunched between the blue and cyan curve. Far away from this critical driving strength ϵ_{cr}, the coherence always decreases ($\epsilon < \epsilon_{\mathrm{cr}}$) or increases ($\epsilon > \epsilon_{\mathrm{cr}}$) monotonously close to $\gamma\tau = 0$, but for $\epsilon \approx \epsilon_{\mathrm{cr}}$, the curves are deformed. The switch from bunched to antibunched and vice versa happens for very small variations of the driving strength. For long time delays, the coherence approaches 1 in any case.

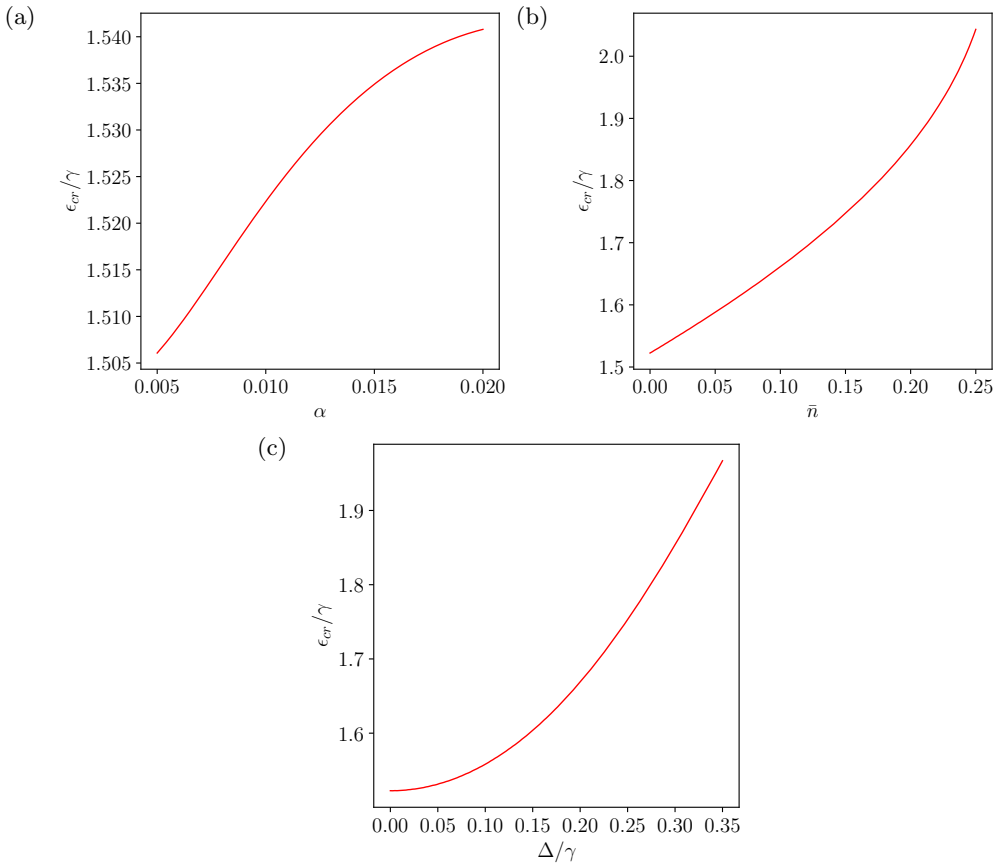

Figure 4.2: Critical point depending on the system parameters α, $\bar{n}$ and Δ. (a) ϵ_{cr} as a function of the coupling constant α at $\bar{n} = \Delta = 0$. The critical point only changes by about 2% while the coupling constant is quadrupled, so the influence of α in this regime is only marginal. ϵ_{cr} increases monotonously with α. (b) Temperature dependence of ϵ_{cr} at $\alpha = 0.01$ and $\Delta = 0$. For low temperatures, the critical point increases linearly with $\bar{n}$. (c) ϵ_{cr} as a function of detuning for $\alpha = 0.01$ and $\bar{n} = 0$. The leading order in Δ is higher than linear.

Chapter 5

Fano factor

5.1 Fluctuation of total photon counts

Rather than instantaneous photon currents, the Fano factor deals with the description of the total number of detector counting events. We therefore define the superoperator $N(t)$ by

$$N(t) = \int_{-t}^{t} d\tau \mathcal{I}(|\tau|) = \gamma \int_{-t}^{t} d\tau (a_+ a_-^\dagger e^{\mathcal{L}|\tau|}) = 2\gamma \int_0^t d\tau (a_+ a_-^\dagger e^{\mathcal{L}\tau}). \tag{5.1}$$

When applied to a state $|\hat{\rho}\rangle$, it counts twice the total number of detector clicks in the time interval $[0, t]$ while the state evolves according to the Lindblad equation. For example, if applied to the steady state $|\tilde{0}\rangle$, the exponential function has no effect and the expectation value of N(t) is just $2\langle\mathcal{I}\rangle_s t$. If $N(t)$ is applied more than once to the steady state, the remaining exponential functions $e^{\mathcal{L}\tau}$ will affect the result because the ket is changed by the operators $a_+ a_-^\dagger$. Therefore, the interpretation of $N(t)^2|\tilde{0}\rangle$ is that it multiplies (twice) the number of photons emitted until time t in the steady state by (twice) the number of photons emitted until time t *after a photon was detected at time 0*. The reason for taking the absolute value of τ and therefore introducing a factor 2 will become apparent in the following consideration.

We are interested in the total number of emitted photons for all times and define $N \coloneqq \lim_{t\to\infty} N(t)$. As is obvious from the expectation value of $N(t)$ in the steady state, this number generally diverges and only makes sense if used to calculate a relative quantity.
The Fano factor is then defined as the ratio of time integrated zero frequency noise S to the mean of the total photon count. As shown in Ref. [9], the noise is given by $S = \langle N\rangle_s + \langle\langle N^2\rangle\rangle_s$, where the double brackets denote the variance $\langle\langle N^2\rangle\rangle = \langle N^2\rangle - \langle N\rangle^2$. With this insight, the Fano factor assumes the form

$$F = \frac{S}{\langle N\rangle_s} = 1 + \frac{\langle\langle N^2\rangle\rangle_s}{\langle N\rangle_s} \tag{5.2}$$

and indicates the total number of photons correlated to a photon emission at $t = 0$. Besides through the interpretation of $N(t)^2$ given above, this can be understood intuitively from the classical point of view: The summand 1 stems from

the self correlation of the initially emitted photon. The second term classically cannot be negative because N is a real number with a non-negative expectation value. If no other photons are correlated to the first one, the covariance in the enumerator vanishes. This corresponds to a Poissonian distribution and therefore coherent light. The Fano factor will be equal to 1. When the covariance increases, more photons are correlated. This is called **super-Poissonian** light because the variance of the photons counted in any given time interval exceeds its mean value. Note that this variance is *not* equal to $\langle\langle N^2 \rangle\rangle_s$. The latter is the covariance between the total photon counts with and without the photon detection at $t = 0$. It determines if detecting a photon increases ($F > 1$), decreases ($F < 1$), or does not affect ($F = 1$) the expectation for the total number of photons. It is important to distinguish between these two concepts.
Classically, the Fano factor cannot be less than 1. But just like for the second-order coherence, quantum mechanics makes this case possible because N is an operator. If $F < 1$, the light is called **sub-Poissonian**. There is no classical analogue and the explanation as the number of correlated photons does not apply either because the photon at $t = 0$ would not be fully self-correlated.

A lot of parallels to the second-order coherence suggest that the two quantities are related to each other. And indeed, with the definition of the Fano factor in Eq. 5.2 and with Eq. 5.1, we find the relation

$$\begin{aligned} F &= 1 + \frac{\langle\tilde{0}|a_+ a_-^\dagger \int d\tau e^{\mathcal{L}|\tau|} a_+ a_-^\dagger \int dt e^{\mathcal{L}|t|}|\tilde{0}\rangle - \langle\tilde{0}|a_+ a_-^\dagger \int dt e^{\mathcal{L}|t|}|\tilde{0}\rangle\langle\tilde{0}|a_+ a_-^\dagger \int d\tau e^{\mathcal{L}|\tau|}|\tilde{0}\rangle}{\langle\tilde{0}|a_+ a_-^\dagger \int dt e^{\mathcal{L}|t|}|\tilde{0}\rangle} \\ &= 1 + \langle\mathcal{I}\rangle_s \int d\tau \left(\frac{\langle\tilde{0}|a_+ a_-^\dagger e^{\mathcal{L}|\tau|} a_+ a_-^\dagger|\tilde{0}\rangle}{\langle\mathcal{I}\rangle_s^2} - 1 \right), \end{aligned} \tag{5.3}$$

where all integrals are taken with respect to the whole real axis. We were able to cancel the t-integrals because the integrands were independent of t after applying $e^{\mathcal{L}|t|}$ to the steady state. Comparing Eq. 5.3 to Eq. 4.18 yields

$$F = 1 + \langle\mathcal{I}\rangle_s \int d\tau \left(g^{(2)}(\tau) - 1 \right) \tag{5.4}$$

and shows why using the absolute value of τ in Eq. 5.1 makes sense in the same way as defining the second-order coherence to be even.
The accordance between the coherence and the Fano factor is now evident. The integrand vanishes for coherent light, thus $F = 1$. We also see the connection between bunched and super-Poissonian light on the one hand as well as antibunched and sub-Poissonian light on the other hand. Nevertheless, they are not completely interchangeable terms because bunching and antibunching only refers to the coherence close to $\tau = 0$ while the whole curve goes into the calculation of the Fano factor.

5.2 Scaling laws close to threshold

Following from the analytical solution of the second-order coherence in Eq. 4.9, the Fano factor for the special case $\Delta = \bar{n} = 0$ takes the form

$$F = 1 + \frac{3\gamma^2\epsilon^2 + \gamma^4}{(\epsilon^2 - \gamma^2)^2} \tag{5.5}$$

and shows a strong monotonous increase with ϵ, diverging for $\epsilon \to \gamma$. This is because the correlation time τ_* of the slow mode in Eq. 4.11 diverges in this limit. As explained above, the correlation between the initial emission and the photon current at later times stems from the fact that the density matrix is altered when the detector registers a counting event. This necessitates an approach of the steady state in the course of which additional photons are emitted through driving. If the time scale of the approach is longer, the total number of correlated counting events grows. This interpretation also explains the different behavior of the Fano factor and the second-order coherence at $\tau = 0$ for increasing values of ϵ. Even though the coherence starts off at lower values for stronger driving, τ_* increases simultaneously so that the number of correlated photon counts for all times is still greater.
For $\epsilon \to 0$ (but with $\epsilon \neq 0$), we obtain that $F \to 2$. In this limit, only a single driving event takes place preceding the initial measurement. Therefore, only 2 photons are correlated, namely the one at $t = 0$ and its 'partner'.
The special case $\epsilon = 0$ yields $F = 2\bar{n} + 1$. This means that the emission of a thermal photon at time 0 is correlated to $\bar{n}$ photons in the future and just as many in the past.

A quick way to calculate the Fano factor numerically is to evaluate the integral in Eq. 5.4 explicitly. For an invertible superoperator A, the integral $\int_{-t}^{t} d\tau e^{A|\tau|}$ is equal to $2(e^{At} - 1)A^{-1}$. We know, however, that the Liouvillian is singular because of the existence of a steady state. The -1 in Eq. 5.4 fixes this problem. To see this, we can use the spectral decomposition with left and right eigenvectors. In the eigenbasis notation for $\mathcal{L}$ from App. A, $\langle\tilde{0}|$ and $|\tilde{0}\rangle$ belong to eigenvalue 0. The other infinitely many eigenvectors are arbitrarily labeled $\langle\tilde{\lambda_i}|$ and $|\tilde{\lambda_i}\rangle$ and have the eigenvalues $\lambda_i \neq 0$ with $\mathrm{Re}\,\lambda_i < 0$ (so that the system is stable). In this way, the integral over the exponential of the Liouvillian can be rewritten as

$$\int_{-\infty}^{\infty} d\tau e^{\mathcal{L}|\tau|} = \int_{-\infty}^{\infty} d\tau |\tilde{0}\rangle\langle\tilde{0}| + 2\left[\sum_{\lambda_i \neq 0} \frac{1}{\lambda_i} e^{\lambda_i \tau} |\tilde{\lambda_i}\rangle\langle\tilde{\lambda_i}|\right]_0^{\infty}. \tag{5.6}$$

Inserting the first term from the 0 eigenspace into Eq. 5.4 leads to

$$\int_{-\infty}^{\infty} d\tau \frac{\langle\tilde{0}|a_+ a_-^\dagger|\tilde{0}\rangle\langle\tilde{0}|a_+ a_-^\dagger|\tilde{0}\rangle}{\langle\mathcal{I}\rangle_s^2} = \int_{-\infty}^{\infty} d\tau 1, \tag{5.7}$$

which cancels the -1 in the integral. The remaining expression for the Fano factor is found by evaluating the second term in Eq. 5.6 and inserting it into

Eq. 5.4 as well. This results in

$$F = \sum_{\lambda_i \neq 0} -\frac{2}{\lambda_i} \frac{\langle \tilde{0}|a_+ a_-^\dagger|\tilde{\lambda_i}\rangle\langle\tilde{\lambda_i}|a_+ a_-^\dagger|\tilde{0}\rangle}{\langle a_+ a_-^\dagger\rangle} = -2\frac{\langle\tilde{0}|a_+ a_-^\dagger P\mathcal{L}^{-1}Pa_+ a_-^\dagger|\tilde{0}\rangle}{\langle a_+ a_-^\dagger\rangle} \tag{5.8}$$

with the projector $P = I - |\tilde{0}\rangle\langle\tilde{0}|$ onto the complement of the 0 eigenspace. The last step is to be understood purely numerically. Only in that way can the analytically singular matrix be inverted before the problematic subspace is removed. For numerical reasons, it is best to avoid inverting matrices. Hence, implementing the calculation of the enumerator in Eq. 5.8 can be done efficiently by defining $|v\rangle \coloneqq Pa_+ a_-^\dagger|\tilde{0}\rangle$, solving the system $\mathcal{L}|w\rangle = |v\rangle$ for $|w\rangle$ and then determining $\langle\tilde{0}|a_+ a_-^\dagger P|w\rangle$.

Fig. 5.1 depicts the Fano factor as a function of ϵ for $\bar{n} = \Delta = 0$. The red curve shows the case without the nonlinear potential, where the solution is given by Eq. 5.5. The coupling constant for the blue curve is $\alpha = 0.01$. Rather than growing indefinitely for increasing driving strengths, the nonlinearity causes F to decrease after reaching a peak. This peak is not right at threshold but shifted toward greater driving strengths. Referring back to Fig. 3.2c from Ch. 3, we can conclude that the peak is positioned at approximately the driving strength where the characteristic time τ_* reaches its maximum, which agrees with our interpretation of Eq. 5.5. Above threshold, the light eventually becomes sub-Poissonian, which is predictable due to the occurrence of photon antibunching for driving strengths of this magnitude. The critical point ϵ_{cr} is a good estimate for when the switch from the super- to the sub-Poissonian regime happens. As explained, the terms are not equivalent to bunching and antibunching, so there is a slight deviation. The quickly deforming coherence function close to ϵ_{cr} results in a discontinuity of the first derivative of $F(\epsilon)$. For $\epsilon \gg \gamma$, the bend in the figure suggests that the light becomes second-order coherent again.

Close to threshold, the Fano factor ($F - 1$, to be precise) follows universal scaling laws, a fact which has been derived in Ref. [3]. We want to use our numerics to verify the predictions. Deviations are to be expected because the theory is accurate in the limit $\alpha \to 0^+$.
$F - 1$ at threshold scales $\propto \alpha^{-1}$ and is independent of $\bar{n}$. The Fano factor has a universal form if plotted against the dimensionless distance $\beta = \frac{1}{2}(\epsilon - \gamma)\tau_*$ from threshold. This means that the peak, for example, is at $\beta = \text{const.}$, so its position scales like τ_*^{-1} if it is viewed as a function of ϵ. The same applies to the FWHM if $\epsilon = \gamma$ is used as the reference position to determine the width of the peak. Following the predictions for the scaling of τ_*, we consequently expect the FWHM to scale $\propto \alpha^{0.5}$ and $\propto (2\bar{n} + 1)^{0.5}$.

Fig 5.2a shows the curves of $F - 1$ depending on the driving strength for six values of α, starting at $\alpha = 0.001$ and doubling for each curve up to $\alpha = 0.032$. $\bar{n}$ and Δ are set to 0. The values of $F - 1$ at $\epsilon = \gamma$ can be determined from the graphs. Their logarithms are plotted against the corresponding values of $\ln(\alpha)$, which is depicted in Fig. 5.3a. The double-logarithmic scale makes it possible to

recognize power laws as linear dependencies and determine the powers through the slope of the line. Such a linear regression has already been performed in Fig. 5.3a. It is to be noted that only the first three points have been used in the regression since the function becomes obviously nonlinear for larger values of α. The same analysis has been done with the FWHM.
Accordingly, Fig. 5.2b shows $F-1$ at $\Delta = 0$ for six values of $\bar{n}$ starting at $\bar{n} = 0.1$ and doubling in each step up to $\bar{n} = 3.2$. The coupling constant has been chosen as $\alpha = 0.004$, a smaller value was not feasible because nonzero temperatures cause the value of n_{max} required for numerical accuracy to grow substantially. We therefore expect higher deviations from the predictions in this case.

Tab. 5.1 lists the obtained results of the linear regression and the expectations for the scaling powers denoted by δ. The deviations from the theory are especially pronounced in the scaling of the FWHM with $(2\bar{n}+1)$, where the relative difference is approximately 20%. However, considering the mentioned numerical limitation, the expectations are generally met with acceptable accuracy. Pinpointing an error for the slopes is not useful because the systematic difference away from $\alpha \to 0^+$ has a greater effect than the exact subjective placement of the linear regression. This is made clear by Fig. 5.3a. The tendency for higher values of α is that the data points are below the regression line. If much smaller values of α were available, we would thus expect a less negative slope, which is confirmed by the theoretical prediction. In contrast, the regression through the first three points has a much higher accuracy.

The determined powers can be used to show that the Fano factor follows a universal form by rescaling the axes. This is done in Fig. 5.3b and Fig. 5.3c for α and $\bar{n}$, respectively. The constants c_1 and c_2 have been chosen so that they normalize the FWHM of the respective first data set to 2 and its value of $(F-1)|_{\epsilon=\gamma}$ to 1 . We see that the curves follow the universal form for the smallest values of α and $\bar{n}$ as expected. For the scaling with α, strong differences occur in the graphs with $\alpha \geq 0.008$, which is right where the linear approximation in Fig. 5.3a breaks down. The curves with different values of $\bar{n}$ start deviating considerably for $\bar{n} \geq 1.6$.

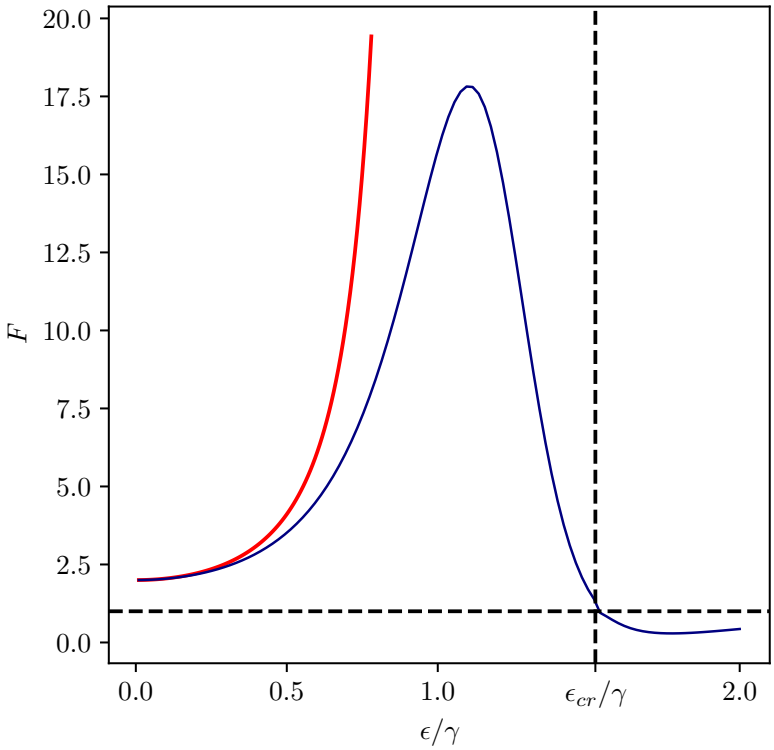

Figure 5.1: Fano factor as a function of driving strength with $\bar{n} = \Delta = 0$ for $\alpha = 0$ (red) and $\alpha = 0.01$ (blue). The horizontal dashed line at $F = 1$ marks the transition from super-Poissonian to sub-Poissonian light. For the blue curve, this transition happens around its critical driving strength marked by the vertical dashed line. Both graphs coincide in the limit $\epsilon \ll \gamma$. But instead of diverging at threshold, the blue curve exhibits a peak, falls below $F = 1$ and approaches it again for $\epsilon \gg \gamma$. The maximum Fano factor is located in the interval given by Fig. 3.2c in which the characteristic time τ_* reaches its highest value.

Scaling law close to threshold	prediction for δ	δ from linear regression
$(F-1)\|_{\epsilon=\gamma} \propto \alpha^{\delta}$	-1	-1.03
FWHM $\propto \alpha^{\delta}$	0.5	0.46
$(F-1)\|_{\epsilon=\gamma} \propto (2\bar{n}+1)^{\delta}$	0	-0.06
FWHM $\propto (2\bar{n}+1)^{\delta}$	0.5	0.60

Table 5.1: Theoretical predictions and results from the linear regression for the scaling laws of $F-1$ and the FWHM close to threshold. Considering that α could not be chosen arbitrarily small (especially for nonzero temperatures), the results are in good accordance with the expectations.

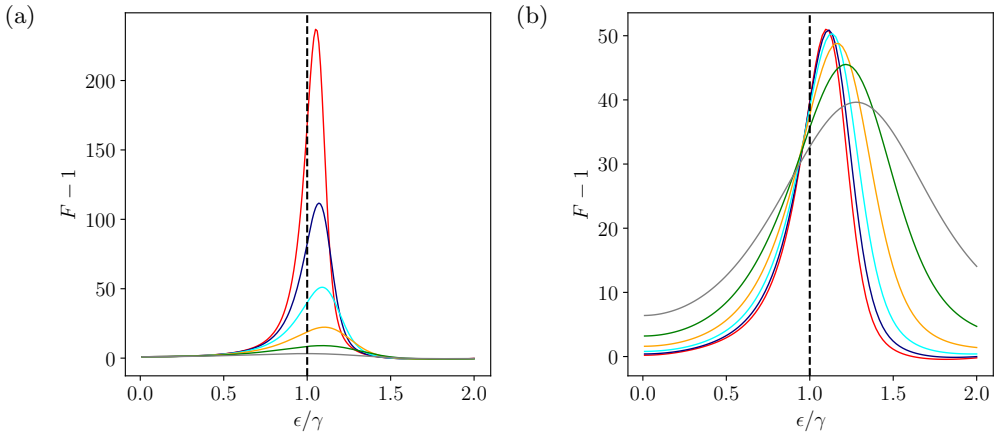

Figure 5.2: Fano factors as a function of driving strength for different coupling constants and temperatures. These data sets are used to verify the scaling laws. The dashed vertical lines mark the threshold $\epsilon = \gamma$ (a) Fano factor for $\bar{n} = \Delta = 0$. The coupling constants of the depicted curves are $\alpha = 0.001$ (red), $\alpha = 0.002$ (blue), $\alpha = 0.004$ (cyan), $\alpha = 0.008$ (orange), $\alpha = 0.016$ (green) and $\alpha = 0.032$ (gray). (b) Fano factor for $\Delta = 0$ and $\alpha = 0.004$. The Bose-Einstein occupations of the depicted curves are $\bar{n} = 0.1$ (red), $\bar{n} = 0.2$ (blue), $\bar{n} = 0.4$ (cyan), $\bar{n} = 0.8$ (orange), $\bar{n} = 1.6$ (green) and $\bar{n} = 3.2$ (gray).

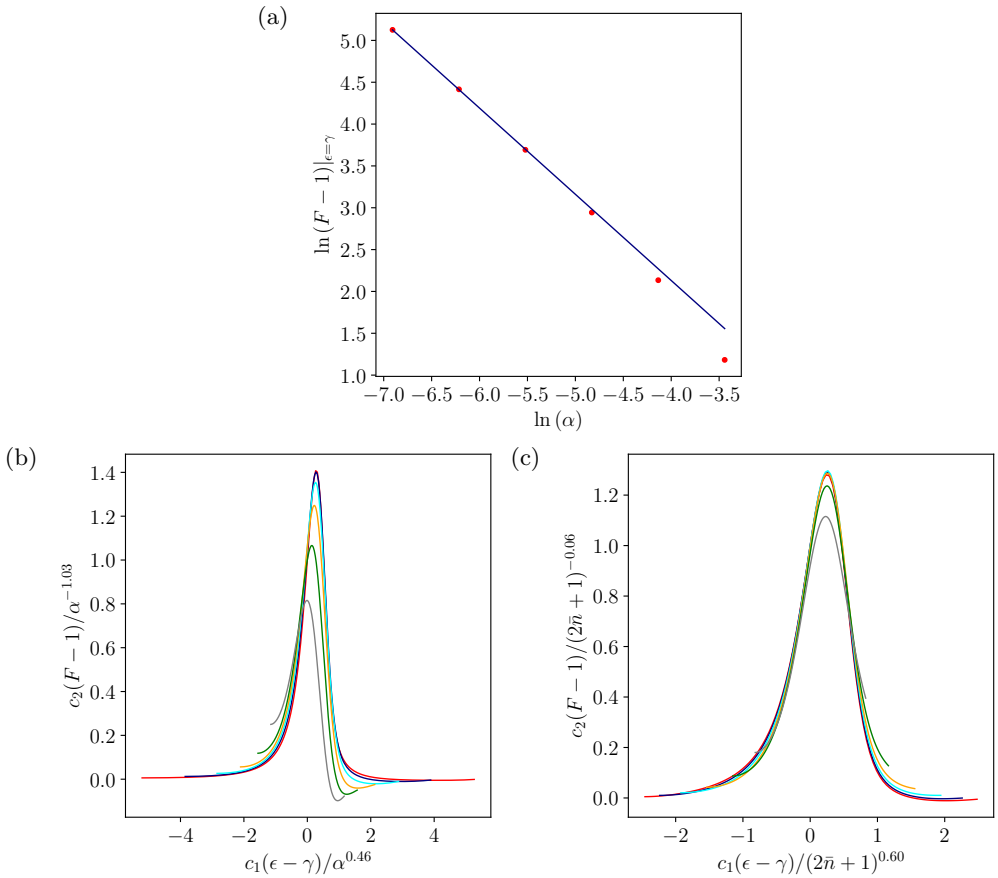

Figure 5.3: Scaling laws and universal form of the Fano factor. (a) Linear regression for the values of $F-1$ at threshold depending on the coupling constant α. Only the first three points follow a linear function in the double logarithmic scale. This particular regression yielded a slope of -1.03, which fits the expectation of $(F-1)|_{\epsilon=\gamma} \propto \alpha^{-1}$. The other linear regressions were done in the same manner and are not explicitly shown here, but the results are listed in Tab. 5.1. (b) and (c) Universal form of the Fano factor for the data sets from Fig. 5.2a and Fig. 5.2b, respectively (the color coding of the curves has remained the same). The axes have been rescaled according to the results of the linear regressions and the x axes were shifted to recreate the universal form as a function of the dimensionless distance β from threshold. The constants c_1 and c_2 were chosen so that the threshold value of $F-1$ is normalized to 1 for the red curves, and their FWHMs are normalized to 2.

Chapter 6

Efficient simulation of the Lindblad equation

Describing the statistical properties of the system by single numbers (like the Fano factor or the critical point) is convenient because they can be calculated numerically without simulating the dynamics of the system. Nevertheless, curves like the second-order coherence that do need to be determined through simulation contain further information. One example is the characteristic correlation time τ_*, which can be extracted from $g^{(2)}(\tau)$ but not from the Fano factor. It is therefore important to find ways of reducing computation times of the simulation.

The starting point is the problem without the nonlinear potential using the superoperator formalism introduced in Ch. 4. A method called Bogoliubov transformation is used to find a new basis in which the Liouvillian is diagonal. To that end, we define four new superoperators u_i and v_i with $i \in \{1, 2\}$ as linear combinations

$$\begin{aligned} u_i &= u_{i1}a_+ + u_{i2}a_- + u_{i3}a_+^\dagger + u_{i4}a_-^\dagger, \\ v_i &= v_{i1}a_+ + v_{i2}a_- + v_{i3}a_+^\dagger + v_{i4}a_-^\dagger \end{aligned} \tag{6.1}$$

of the Fock basis superoperators. The goal now is to determine the coefficients in a way that creates a bosonic structure for the Liouvillian, i.e.

$$\mathcal{L} = \lambda_1 v_1 u_1 + \lambda_2 v_2 u_2, \tag{6.2}$$

where the v_i act as new creation operators and the u_i as annihilation operators. Because the Liouvillian is not Hermitian, u_i is not the adjoint of v_i. The bosonic structure can be induced by demanding that the operators fulfill the commutation relations

$$\begin{aligned} [\mathcal{L}, u_i] &= -\lambda_i u_i, \\ [\mathcal{L}, v_i] &= \lambda_i v_i, \\ [u_i, v_j] &= \delta_{ij}, \end{aligned} \tag{6.3}$$

which are known, e.g., from a two-dimensional harmonic oscillator. After finding these operators, a new basis with two labels can be used, consisting of states

$|n,m\rangle$ that are eigenstates of $\mathcal{L}$ with eigenvalue $n\lambda_1 + m\lambda_2$.

In order to gather conditions for the coefficients, the commutation relations

$$\begin{aligned}[a_+, a_+^\dagger] &= 1, \\ [a_-, a_-^\dagger] &= -1\end{aligned} \tag{6.4}$$

for the Fock basis superoperators are needed. The commutators between all other pairings vanish. These relations and Eq. 4.16 can be used in Eq. 6.3. If the u_i and v_i are represented by the column vectors

$$\begin{aligned}\boldsymbol{u_i} &= \begin{pmatrix} u_{i1} & u_{i2} & u_{i3} & u_{i4} \end{pmatrix}^T, \\ \boldsymbol{v_i} &= \begin{pmatrix} v_{i1} & v_{i2} & v_{i3} & v_{i4} \end{pmatrix}^T,\end{aligned} \tag{6.5}$$

the first two commutation relations from Eq. 6.3 are equivalent to the eigenvalue problems

$$\begin{aligned}\underline{\mathrm{M}}\boldsymbol{u_i} &= \lambda_i \boldsymbol{u_i}, \\ \underline{\mathrm{M}}\boldsymbol{v_i} &= -\lambda_i \boldsymbol{v_i}\end{aligned} \tag{6.6}$$

with the matrix $\underline{\mathrm{M}}$ given by

$$\underline{\mathrm{M}} = \begin{pmatrix} -i\frac{\Delta}{2} - \gamma(\bar{n}+\frac{1}{2}) & -\gamma(\bar{n}+1) & \frac{\epsilon}{2} & 0 \\ \gamma\bar{n} & -i\frac{\Delta}{2} + \gamma(\bar{n}+\frac{1}{2}) & 0 & \frac{\epsilon}{2} \\ \frac{\epsilon}{2} & 0 & i\frac{\Delta}{2} + \gamma(\bar{n}+\frac{1}{2}) & \gamma\bar{n} \\ 0 & \frac{\epsilon}{2} & -\gamma(\bar{n}+1) & i\frac{\Delta}{2} - \gamma(\bar{n}+\frac{1}{2}) \end{pmatrix}. \tag{6.7}$$

The four eigenvalues of $\underline{\mathrm{M}}$ are

$$\lambda_{\pm\pm} = \pm\frac{1}{2}\sqrt{(\gamma^2 + \epsilon^2 - \Delta^2) \pm 2\gamma\sqrt{\epsilon^2 - \Delta^2}} \tag{6.8}$$

and appear in pairs with different signs. The set of eigenvectors of $\underline{\mathrm{M}}$ contains all four vectors $\boldsymbol{u_i}$ and $\boldsymbol{v_i}$ since the operators with identical indices obey the same eigenvalue problem for the sign-switched eigenvalue (c.f. Eq. 6.6). If the sign of $\lambda_{\pm+}$ and $\lambda_{\pm-}$ is chosen and they are identified with λ_1 and λ_2, this fixes the complete form of the operators u_i and v_i (up to a prefactor).
Now that we have shown this fact in the most general case, we will focus on $\Delta = 0$. The eigenvalues reduce to

$$\lambda_{\pm\pm} = \pm\frac{1}{2}(\gamma \pm \epsilon) \tag{6.9}$$

and the corresponding eigenvectors $\boldsymbol{w}_{\pm\pm}$ are given by

$$\boldsymbol{w}_{++} = \begin{pmatrix} -1 \\ 1 \\ -1 \\ 1 \end{pmatrix}; \boldsymbol{w}_{+-} = \begin{pmatrix} 1 \\ -1 \\ -1 \\ 1 \end{pmatrix}; \boldsymbol{w}_{-+} = \begin{pmatrix} 1 \\ \frac{\epsilon+2\gamma\bar{n}}{\epsilon-2\gamma(\bar{n}+1)} \\ \frac{\epsilon+2\gamma\bar{n}}{\epsilon-2\gamma(\bar{n}+1)} \\ 1 \end{pmatrix}; \boldsymbol{w}_{--} = \begin{pmatrix} -1 \\ \frac{-\epsilon+2\gamma\bar{n}}{\epsilon+2\gamma(\bar{n}+1)} \\ \frac{\epsilon-2\gamma\bar{n}}{\epsilon+2\gamma(\bar{n}+1)} \\ 1 \end{pmatrix}. \tag{6.10}$$

The last commutation relation in Eq. 6.3 can be interpreted as an orthonormality condition for the eigenvectors. But rather than the Euclidean inner product, the modified dot product

$$(\boldsymbol{a}, \boldsymbol{b}) \coloneqq \boldsymbol{a}^T \begin{pmatrix} 0 & 0 & 1 & 0 \\ 0 & 0 & 0 & -1 \\ -1 & 0 & 0 & 0 \\ 0 & 1 & 0 & 0 \end{pmatrix} \boldsymbol{b} \tag{6.11}$$

with an inserted metric matrix induces the norm. It is not commutative [1], so we need to choose the signs of the eigenvalues before the normalization can be executed in the right order, i.e. $(\boldsymbol{u}_i, \boldsymbol{v}_j) = \delta_{ij}$.
All four possible combinations of assigning $\lambda_{\pm+} \to \lambda_1$ and $\lambda_{\pm-} \to \lambda_2$ are valid in that the correct Liouvillian is obtained. We know that the system is stable and can therefore already guess that the combination with both negative eigenvalues is the correct one. Otherwise the time evolution in the new basis $e^{\mathcal{L}t}|n,m\rangle = e^{(n\lambda_1+m\lambda_2)t}|n,m\rangle$ diverges for certain choices of m and n. This guess can be proven using the trace preserving property of the Lindblad equation (Eq. 2.16). With the basis independent insight of App. A, it can be written as

$$\langle 0,0|\mathcal{L}|\hat{\rho}\rangle = 0 \tag{6.12}$$

for an arbitrary, not necessarily normalized state $|\hat{\rho}\rangle$. Inserting Eq. 6.2 leads to the condition

$$\lambda_1 \langle 0,0|v_1|\hat{\rho}_1\rangle + \lambda_2 \langle 0,0|v_2|\hat{\rho}_2\rangle = 0, \tag{6.13}$$

where we have defined $|\hat{\rho}_1\rangle \coloneqq u_1|\hat{\rho}\rangle$ and $|\hat{\rho}_2\rangle \coloneqq u_2|\hat{\rho}\rangle$. Since $|\hat{\rho}\rangle$ is arbitrary, so are $|\hat{\rho}_1\rangle$ and $|\hat{\rho}_2\rangle$. Thus, both terms have to vanish independently. This shows that the v_i have to be of the form $c_1(a_+ - a_-) + c_2(a_+^\dagger - a_-^\dagger)$ because their trace vanishes by cyclic permutation. As a consequence, we can identify the eigenspaces through the proportionalities

$$\begin{aligned} \boldsymbol{v}_1 &\propto \boldsymbol{w}_{++}, \\ \boldsymbol{u}_1 &\propto \boldsymbol{w}_{-+}, \\ \boldsymbol{v}_2 &\propto \boldsymbol{w}_{+-}, \\ \boldsymbol{u}_2 &\propto \boldsymbol{w}_{--}. \end{aligned} \tag{6.14}$$

The appropriate eigenvalues are $\lambda_1 = \lambda_{-+}$ and $\lambda_2 = \lambda_{--}$.
Now that the eigenspaces are assigned, the normalization with the dot product from Eq. 6.11 can be performed in the correct order. The orthogonality is already satisfied by the eigenvectors, so the remaining two conditions

$$(\boldsymbol{w}_{-+}, a\boldsymbol{w}_{++}) = (\boldsymbol{w}_{--}, b\boldsymbol{w}_{+-}) = 1 \tag{6.15}$$

specify the constants a and b in $\boldsymbol{v}_1 = a\boldsymbol{w}_{++}$ and $\boldsymbol{v}_2 = b\boldsymbol{w}_{+-}$, while the other two proportionality constants in Eq. 6.14 are set to 1.

[1] Instead, it is anticommutative.

The fact that the simultaneous transformations $u_i \to \widetilde{u_i} = a u_i$ and $v_i \to \widetilde{v_i} = a^{-1} v_i$ for any number a does not change Eq. 6.2 allows shuffling constants between the operators with the same index.
Taking everything into account finally leads to

$$\begin{aligned}
\mathcal{L} &= \lambda_1 v_1 u_1 + \lambda_2 v_2 u_2, \\
\lambda_1 &= -\frac{\gamma+\epsilon}{2}, \\
\lambda_2 &= -\frac{\gamma-\epsilon}{2}, \\
v_1 &= -a_+ + a_- - a_+^\dagger + a_-^\dagger, \\
v_2 &= a_+ - a_- - a_+^\dagger + a_-^\dagger, \\
u_1 &= \frac{\epsilon + 2\gamma(\bar{n}+1)}{4(\gamma+\epsilon)}(a_-^\dagger - a_+) + \frac{\epsilon - 2\gamma\bar{n}}{4(\gamma+\epsilon)}(a_+^\dagger - a_-), \\
u_2 &= \frac{\epsilon - 2\gamma(\bar{n}+1)}{4(\gamma-\epsilon)}(a_-^\dagger + a_+) + \frac{\epsilon + 2\gamma\bar{n}}{4(\gamma-\epsilon)}(a_+^\dagger + a_-).
\end{aligned} \tag{6.16}$$

It is known how the new creation and annihilation operators act on a state up to a prefactor, i.e. $u_1|n,m\rangle \sim |n-1,m\rangle$. While this prefactor is determined in Fock space through the fact that $\hat{a}$ and $\hat{a}^\dagger$ are adjoint operators ($\langle n|\hat{a}^\dagger\hat{a}|n\rangle = n = |\hat{a}|n\rangle|^2$), it can be freely distributed between u_i and v_i as long as the eigenvalue of $v_i u_i$ is the according occupation number. One possible choice is to keep the same distribution, so that $u_1|n,m\rangle = \sqrt{n}|n-1,m\rangle$, $v_1|n,m\rangle = \sqrt{n+1}|n+1,m\rangle$ and analogously for u_2 and v_2. We will use this convention in the remainder of the chapter.

It is helpful for calculations to express the Fock basis superoperators as

$$\begin{aligned}
a_+ &= -(\epsilon - 2\gamma\bar{n})v_1 - (\epsilon + 2\gamma\bar{n})v_2 - \frac{1}{4(\gamma+\epsilon)}u_1 - \frac{1}{4(\gamma-\epsilon)}u_2, \\
a_- &= [\epsilon + 2\gamma(\bar{n}+1)]\, v_1 + [\epsilon - 2\gamma(\bar{n}+1)]\, v_2 - \frac{1}{4(\gamma+\epsilon)}u_1 - \frac{1}{4(\gamma-\epsilon)}u_2, \\
a_+^\dagger &= -[\epsilon + 2\gamma(\bar{n}+1)]\, v_1 + [\epsilon - 2\gamma(\bar{n}+1)]\, v_2 + \frac{1}{4(\gamma+\epsilon)}u_1 - \frac{1}{4(\gamma-\epsilon)}u_2, \\
a_-^\dagger &= (\epsilon - 2\gamma\bar{n})v_1 - (\epsilon + 2\gamma\bar{n})v_2 + \frac{1}{4(\gamma+\epsilon)}u_1 - \frac{1}{4(\gamma-\epsilon)}u_2
\end{aligned} \tag{6.17}$$

using Eq. 6.16. For consistency, one can check that the result of $\langle \mathcal{I} \rangle_s = \langle 0,0|a_+ a_-^\dagger|0,0\rangle$ is equal to Eq. 3.5. To this end, all combinations of u_i and v_i in $a_+ a_-^\dagger$ that change the ket $|0,0\rangle$ or apply an annihilation operator to it can be ignored.
In the same way, the second-order coherence

$$g^{(2)}(\tau) = \frac{\langle 0,0|a_+ a_-^\dagger e^{\mathcal{L}|\tau|} a_+ a_-^\dagger|0,0\rangle}{\langle 0,0|a_+ a_-^\dagger|0,0\rangle^2} \tag{6.18}$$

is found to be the same as in Eq. 4.11. This shows that the introduced method is also helpful in analytical calculations. Once the operators in Eq. 6.16 are

obtained, the solutions to many of the previous problems can be found without the need to solve linear systems.

The basis $\{|n,m\rangle\}$ can be used for an approach toward a more efficient simulation method. In the linear problem, the mode $|n,m\rangle$ decays with a rate of $R_{nm} \coloneqq |n\lambda_1 + m\lambda_2|$ (in the general case, the real part of the eigenvalues has to be taken, but we are still focusing on $\Delta = 0$). If the anharmonicity is added, the decay behavior of $|n,m\rangle$ is changed. Also, $|0,0\rangle$ is not the steady state anymore. It is rather a linear combination of different kets. However, in the limit $\alpha \to 0^+$, the properties of the linear system should be restored. Therefore, if α is chosen sufficiently small, modes with a high decay rate R can be ignored because they do not appear in the simulation of the linear problem (Eq. 6.18 contains only modes with at most four total excitations) and also decay fast compared to the simulation time scale. We thus define a **maximum decay rate $\boldsymbol{\Gamma > 0}$**. Γ replaces the parameter n_{max} from the Fock basis, and we expect to get accurate results in the limit $\Gamma \gg \gamma$.

Below threshold, all modes $|n,m\rangle$ with $R_{nm} > \Gamma$ are removed from the matrices. This can be done by initially choosing the dimension $\dim_i$ large enough so that all relevant modes are included, for example $\dim_i = \left\lceil \frac{\Gamma}{\min(|\lambda_1|,|\lambda_2|)} \right\rceil + 1$. The matrix representations of u_i and v_i in the new basis are the same as those of the Fock basis superoperators. For example, the matrix for $v_1 = v \otimes 1$ is given by that of $a_+^\dagger$ in the Fock basis. After the initial definition, every subspace with occupation numbers n and m is examined. If $R_{nm} > \Gamma$, the $(n\dim_i + m)$th[2] row and column are removed from all matrices as well as the $(n\dim_i + m)$th element from the trace and steady state.
Above threshold, another parameter has to be introduced to limit the number of m in $|n,m\rangle$ because the eigenvalue λ_2 is positive. This parameter, which we call M_{max}, is necessary because without it, the condition $R_{nm} \leq \Gamma$ could always be fulfilled by including a high enough multiple of λ_2. For the same reasons as below threshold, the results should converge to the exact solution in the joint limit $\Gamma \gg \gamma$ and $M_{max} \to \infty$.

Below threshold, the method yields good results. It becomes apparent that not many modes are needed to approximate the time evolution of the system. Hence, the computation time is reduced. As an example, Fig. 6.1 shows the coherence simulated with the new method for a fixed set of parameters and how it changes with increasing values of Γ. We see that the result converges to the black curve, which is the solution simulated in the Fock basis with high enough n_{max} to obtain numerical accuracy. Also, the long term behavior $\gamma\tau \gg 1$ coincides with the approximations even for lower values of Γ because the discarded modes have already decayed in that regime. The coherence with the highest used value of $\Gamma = 3\gamma$ has converged, and the matrices in that case are only of dimension 39×39 while the corresponding matrices in the Fock basis need to be approximately of dimension 150×150 to reach convergence. This demonstrates

[2] C.f. App. A for the correspondence between tensor products and matrix elements.

that the new basis allows for much more efficient simulations.

Above threshold, the method fails to yield the correct steady state density matrix, even if α is chosen very small and Γ and M_{max} very large. For example, a negative photon current is calculated from the determined left and right eigenvectors with eigenvalue 0. The calculation of eigenvectors converges however, which hints at a deeper root of the difficulties. There seem to be two numerical problems which might be connected with each other. For one, the spectrum of the Liouvillian contains positive eigenvalues. An example of such a spectrum is shown in Fig. 6.2a. Even if the correct steady state density matrix was obtained, this would lead to a diverging time evolution. Furthermore, Fig. 6.2b depicts the absolute values of the elements in the density matrix with eigenvalue 0, before removing the modes with high decay rates. The weight of the probability distribution shifts toward the highest allowed occupation of the slowly decaying mode. The colors change on a logarithmic scale, so the values at the boundary diverge, reaching magnitudes of more than 10^{20}. Simply removing these subspaces is not enough because the steady state might already be distorted. Cutting the subspaces from the Liouvillian *before* finding the eigenvectors does also not lead to the correct result.

Several approaches did not yet succeed in but might provide a starting point for recovering the correct solution. One idea is to remove the eigenspaces of positive eigenvalues with projectors of the form $P = 1 - |\tilde{\lambda}\rangle\langle\tilde{\lambda}|$ from the Liouvillian by setting $\tilde{\mathcal{L}} = P\mathcal{L}P$. While this might counteract the divergence of the modes in the time evolution, it does not yield the correct steady state. Secondly, the accumulation of the weight in the density matrix at the cutoff could necessarily appear as long as the dimension is artificially set to a finite value. The problem may be overcome by introducing jump operators with the same form as the dissipator in Eq. 2.13 into the Liouvillian. While the dissipator lowers the occupation number in the Fock basis by 1, jump operators that shift the weight of the steady state from the boundary toward lower modes can be constructed. This idea needs more consideration, because simply adding such operators that cause a probability flow to the state $|0, 0\rangle$ does not change the wrong result. It is possible that more mathematical insight into the structure of problems with infinite dimension and their numerical, thus finite implementation can help to extend the ideas presented.

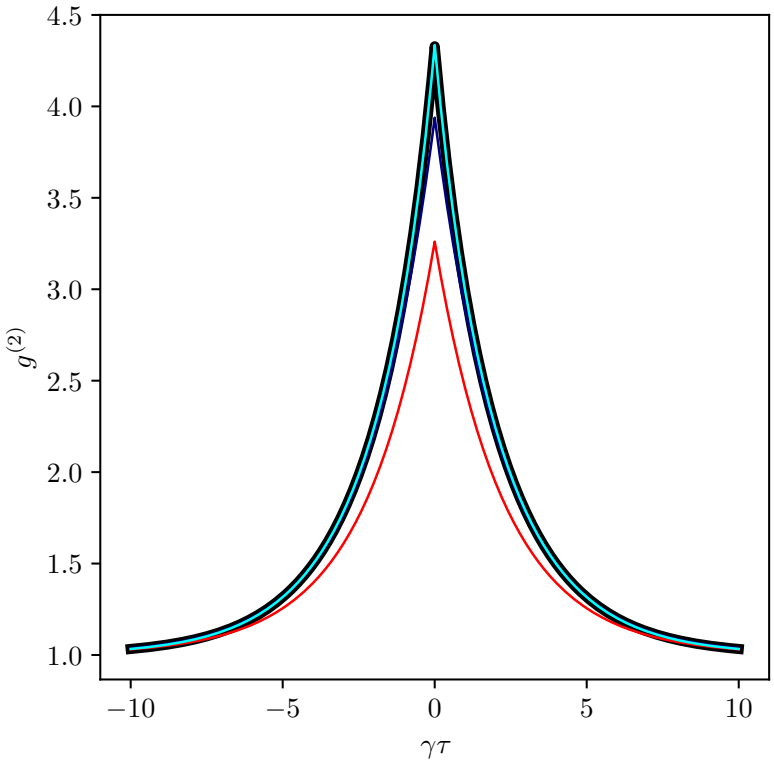

Figure 6.1: Second-order coherence with the new simulation method for $\epsilon = 0.6$, $\alpha = 0.01$ and $\bar{n} = \Delta = 0$. The thick black curve is the result obtained in the Fock basis, where convergence has definitely been reached. The different maximum decay rates of $\Gamma = 0.5\gamma$ (red), $\Gamma = \gamma$ (blue) and $\Gamma = 3\gamma$ show that the correct result is obtained by increasing Γ. Also, the graphs with lower values of Γ still become accurate for $\gamma\tau \gg 1$ because the cropped modes decay more quickly.

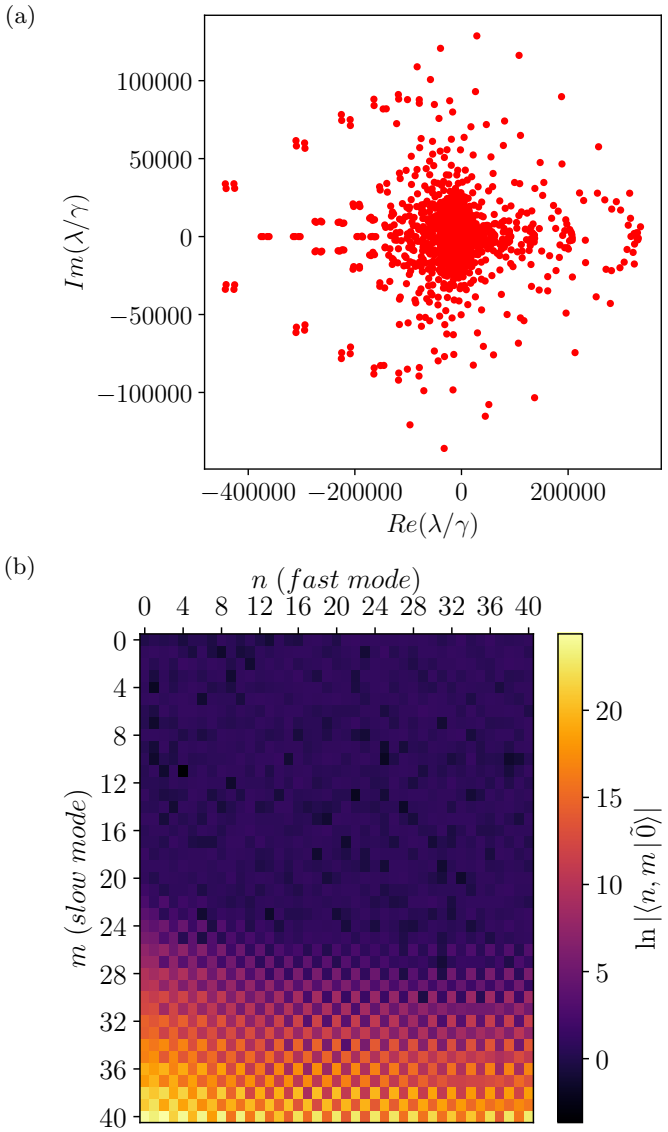

Figure 6.2: Spectrum and steady state density operator from the numerical implementation of the new basis above threshold. Both figures have been created with parameters $\epsilon = 1.2\gamma$, $\alpha = 0.01$, and $\Delta = \bar{n} = 0$. The matrices were not altered by removing modes, they have the initial dimension $\dim_i^2 \times \dim_i^2$. $\Gamma = 20\gamma$ and $M_{max} = 40$ have been chosen particularly large to show that they are not the cause of the wrong results. (a) Partial spectrum of the Liouvillian above threshold. Numerous eigenvalues with a highly positive real part occur, and they do not seem to appear in complex conjugate pairs compared to the eigenvalues with a negative real part. The former means that the time evolution with $\mathcal{L}$ as its generator would diverge if it were performed. (b) Weight of the modes $|n, m\rangle$ in the eigenvector of $\mathcal{L}$ with eigenvalue 0. Each square is colored according to the logarithmized absolute value of the expansion coefficient $\langle n, m|\tilde{0}\rangle$. The occupation number n of the quickly decaying mode increases along the x axis, that of the slowly decaying mode (m) along the y axis. The weight of the modes grows exponentially as the slow mode's occupation increases, leading to diverging absolute values. Setting the matrix dimension to a finite size seems to cause numerical difficulties in obtaining the right steady state.

Chapter 7

Conclusion and outlook

In this thesis, we have analyzed the statistical properties of the radiation emitted by a quantum parametric oscillator, mainly regarding the fluctuation and correlation of the photons.
The basic setup of the system and the time evolution for open quantum systems have been explained in Ch. 2. In Ch. 3, we have shown that the parametric oscillator experiences an instability at a driving strength of $\epsilon_{\text{thr}} = \sqrt{\Delta^2 + \gamma^2}$, which is cured by a nonlinear potential. The characteristic time τ_* after which the steady state is reached was found not to be a monotonous function of the driving strength. Instead, it experiences a maximum at a certain value of ϵ.
The second-order coherence has been introduced in Ch. 4 and determined for the case of the parametric oscillator. It has lead to the realization that τ_* is not only the time for the approach of the steady state, but also the typical correlation time for photon emissions. We have demonstrated that the emitted radiation is bunched up to a critical driving strength ϵ_{cr}, where it suddenly turns antibunched. The shifting of this critical point has been simulated, e.g., for changing temperature and the results explained qualitatively. The fact that antibunched light is emitted at all is testimony to the quantum nature of light.
Closely related to the coherence, Ch. 5 has dealt with the Fano factor as a single indicator for the counting statistics of a system. We have seen that the switch from bunched to antibunched light is accompanied by the counting statistics turning sub-Poissonian. While ϵ_{cr} is far away from threshold, the Fano factor takes on a universal form close to threshold, which we have been able to verify numerically. Deviations arise as expected when the coupling constant α of the nonlinearity is increased.
In Ch. 6, the Liouvillian without the nonlinear potential has been diagonalized using a Bogoliubov transformation. The results can be applied to simulate the Lindblad equation more efficiently below threshold if α is chosen small enough. Only the modes with the longest characteristic times are used to describe the dynamics of the system, which reduces computation times significantly.

The thesis raises interesting questions for further consideration. The obvious one is how to extend the efficient simulation method from Ch. 6 above threshold. As mentioned, the answer may lie in choosing appropriate jump operators or

otherwise finding the right boundary conditions so as not to alter the system dynamics when cutting off the matrix dimension. Since the method allows for much faster simulation times, it is worthwhile studying how similar problem have been tackled mathematically in the past.
Another possible next step could be to gather a better understanding of the critical driving strength. The emitted light at ϵ_{cr} is (almost) second-order coherent. This might be a starting point for an analytical approximation based on properties of coherent light that facilitate calculations.

Appendix A

Vectorization of the density operator

The set of $n \times n$ matrices over $\mathbb{C}$ with a norm induced by the inner product $\langle A, B\rangle_{HS} \coloneqq \mathrm{tr}\,(A^\dagger B)$ forms a Hilbert space for any finite value of n. While this notion is complicated a lot when the dimension of the matrices is infinite, it can be shown that density operators in particular are so called trace-class operators. They form a Hilbert space with the same inner product $\langle \cdot, \cdot \rangle_{HS}$, which is called the Hilbert-Schmidt inner product (c.f. Ref. [10]). We denote the Hilbert space of density operators by $\tilde{\mathcal{H}}$.
In the Dirac notation, this allows identifying density operators with kets. After choosing a basis $\{|n\rangle \ , n \in \mathbb{N}_0\}$ of $\mathcal{H}$, a density operator is represented by a linear combination of outer products $|n\rangle\langle m|$. They can be assigned to the tensor products $|n\rangle \otimes |m\rangle$, which are the basis elements of the operator vector space. This means that the density operator $\hat{\rho}$ represented by the matrix

$$\begin{pmatrix} \rho_{0,0} & \rho_{0,1} & \cdots \\ \rho_{1,0} & \rho_{1,1} & \cdots \\ \vdots & \vdots & \ddots \end{pmatrix} \tag{A.1}$$

is identified with the column vector

$$\begin{pmatrix} \rho_{0,0} & \rho_{0,1} & \cdots & \rho_{1,0} & \rho_{1,1} & \cdots & \cdots \end{pmatrix}^T \tag{A.2}$$

by stacking its rows on top of each other. Analytically, the dots stand for infinitely many elements, but the numerical representation of the density matrix has a shape of $n_{\max} \times n_{\max}$. Therefore, the density operator vector space is of dimension $n_{\max}^2$.
Now that the density matrices are established as 'kets' (column vectors), the question is whether or not 'bras' (row vectors) have an interpretation as well. For the row vector given by

$$\sum_{n=0}^{\infty} \langle n| \otimes \langle n| = \begin{pmatrix} 1 & 0 & 0 & \cdots & 0 & 1 & 0 & \cdots & \cdots \end{pmatrix}, \tag{A.3}$$

it is apparent that multiplying it with any vectorized matrix yields its trace.

The creation and annihilation operators can be expressed as matrices in this formalism. Because the tensor product does not commute, the matrices have a different form depending on whether the operators are applied from the left or from the right. For that reason, normal ordering can be denoted in a natural way with different superoperators.
The tensor product between two matrices multiplies each element of the first matrix by the second matrix. The superoperators are thus of the form

$$\begin{aligned} a_+ = \hat{a} \otimes \hat{1} &\doteq \begin{pmatrix} \underline{0} & \underline{\sqrt{1}} & \underline{0} & \cdots \\ \underline{0} & \underline{0} & \underline{\sqrt{2}} & \cdots \\ \underline{0} & \underline{0} & \underline{0} & \cdots \\ \vdots & \vdots & \vdots & \ddots \end{pmatrix}, \\ a_- = \hat{1} \otimes \hat{a}^\dagger &\doteq \begin{pmatrix} \underline{\mathrm{a}}^\dagger & \underline{0} & \underline{0} & \cdots \\ \underline{0} & \underline{\mathrm{a}}^\dagger & \underline{0} & \cdots \\ \underline{0} & \underline{0} & \underline{\mathrm{a}}^\dagger & \cdots \\ \vdots & \vdots & \vdots & \ddots \end{pmatrix}, \end{aligned} \tag{A.4}$$

where the underscores stand for the $n_{max} \times n_{max}$ matrix representation of an operator (c.f. Eq. 3.8) and the numbers are to be understood as multiplied by the identity operator. The two other superoperators from Eq. 4.15 are represented by the adjoint matrices in this basis.

In contrast to the Hamiltonian, the Liouvillian is not a Hermitian operator. As a consequence, the left and right eigenvectors are not the adjoint of each other and have to be determined separately. We use the notation $|\tilde{\lambda}\rangle$ and $\langle\tilde{\lambda}|$ to denote right and left eigenvectors of $\mathcal{L}$ with eigenvalue λ.
A left and a right eigenvector with different eigenvalues are always orthogonal to each other. For $\lambda' \neq \lambda$, we find that

$$(\mathcal{L} - \lambda)|\tilde{\lambda}\rangle = 0 \implies \langle\tilde{\lambda}'|\mathcal{L} - \lambda|\tilde{\lambda}\rangle = 0 \implies (\lambda' - \lambda)\langle\tilde{\lambda}'|\tilde{\lambda}\rangle = 0, \tag{A.5}$$

and since the eigenvalues are different, the bra and the ket are orthogonal. An orthonormality condition for the left and right eigenvectors can therefore be imposed[1], so that

$$\langle\tilde{\lambda}'|\tilde{\lambda}\rangle = \delta_{\lambda',\lambda}. \tag{A.6}$$

The ket $|\tilde{0}\rangle$ is the steady state $|\hat{\rho}_s\rangle$ because the derivative $\frac{d}{dt}|\tilde{0}\rangle = \mathcal{L}|\tilde{0}\rangle = 0$ vanishes. Also, we have found in Eq. 2.16 that the Lindblad equation is

[1] There are some mathematical subtleties involved in proving this rigorously. For example, it must be shown that left and right eigenvectors with the same eigenvalue are not orthogonal. This proof is found in most introductory linear algebra literature. Also, the general property that the eigenvalues of the Liouvillian are real or appear in complex conjugate pairs (Ref. [11]) shows that the sets of left and right eigenvalues are identical.

trace-preserving. The trace is a continuous linear form in the Hilbert space $\tilde{\mathcal{H}}$. According to the Riesz representation theorem, a unique element $\langle \mathrm{tr} \,|$ must appear in the dual space $\tilde{\mathcal{H}}^*$ (the space spanned by the left eigenvectors) so that $\mathrm{tr}\,(\hat{\rho}) = \langle \mathrm{tr} \,|\hat{\rho}\rangle$ for any density matrix $\hat{\rho}$. The trace preservation $\frac{d}{dt}\,\mathrm{tr}\,(\hat{\rho}) = \langle \mathrm{tr} \,|\mathcal{L}|\hat{\rho}\rangle = 0$ identifies $\langle \mathrm{tr} \,| \equiv \langle \tilde{0}|$ due to the arbitrary choice of $\hat{\rho}$. We know the form of the trace in this specific basis (Eq. A.3), but the two key facts that the left and right eigenvectors with eigenvalue 0 are the trace and the steady state are independent of the basis representation.
The normalization Eq. A.6 ensures that the steady state density matrix has unity trace and that all other eigenvectors of the Liouvillian are traceless. The latter is necessary because these modes decay exponentially, so Eq. 2.16 would be violated if they had a nonzero trace.

Acknowledgements

I want to thank Prof. Dr. Fabian Hassler and Steven Kim for the close supervision and for introducing me to the basics of this fascinating research area. The meetings and Zoom calls have always been very insightful and motivating.
I also want to thank Prof. Dr. Markus Müller for being the second referee for my thesis.

Finally, I am more than grateful for my parents, who supported me throughout my bachelor's studies and who I know I can always count on.

Bibliography

[1] Bernard Yurke et al. Observation of 4.2-k equilibrium-noise squeezing via a josephson-parametric amplifier. *Phys. Rev. Lett.*, 60:764–767, 1988.

[2] Roman Schnabel. Squeezed states of light and their applications in laser interferometers. *Physics Reports*, 684:1–51, 2017.

[3] Fabian Hassler, Steven Kim, and Lisa Arndt. Radiation statistics of a degenerate parametric oscillator at threshold. *SciPost Phys.*, 14:156, 2023.

[4] Göran Lindblad. *On the Generators of Quantum Dynamical Semigroups.* Springer, Communications in Mathematical Physics, 1976.

[5] Heinz-Peter Breuer and Francesco Petruccione. *The Theory of Open Quantum Systems.* Oxford University Press, 2002.

[6] Maria G. Westdickenberg. *Höhere Mathematik 2 (German lecture script)[Higher mathematics 2].* 2021.

[7] Rodney Loudon. *The Quantum Theory of Light.* Oxford University Press, 2001.

[8] Mark Fox. *Quantum Optics:An Introduction.* Oxford University Press, 2006.

[9] Clive Emary et al. Bunching and antibunching in electronic transport. *Phys. Rev. B*, 85:165417, 2012.

[10] John B. Conway. *A Course in Functional Analysis.* Springer, 1990.

[11] Steven Kim and Fabian Hassler. Third quantization for bosons: symplectic diagonalization, non-hermitian hamiltonian, and symmetries. 2023.